



Metal-organic framework-mediated siRNA delivery and sonodynamic therapy for precisely triggering ferroptosis and augmenting ICD in osteosarcoma

Ningxiang Sun^{a,1}, Qingjian Lei^{a,1}, Meng Wu^{b,1}, Shijie Gao^a, Zhiqiang Yang^a, Xuan Lv^a, Renxiong Wei^{a,**}, Feifei Yan^{a,***}, Lin Cai^{a,*}

^a Department of Spine Surgery and Musculoskeletal Tumor, Zhongnan Hospital of Wuhan University, 168 Donghu Street, Wuchang District, Wuhan, Hubei, 430071, China

^b Department of Ultrasound, Zhongnan Hospital of Wuhan University, 168 Donghu Street, Wuchang District, Wuhan, Hubei, 430071, China

ARTICLE INFO

Keywords:

siRNA delivery
Metal-organic framework
Ferroptosis
Sonodynamic therapy
Osteosarcoma

ABSTRACT

The complex genomics, immunosuppressive tumor microenvironment (TME), and chemotherapeutic resistance of osteosarcoma (OS) have resulted in limited therapeutic effects in the clinic. Ferroptosis is involved in tumor progression and is regulated mainly by glutathione peroxidase 4 (GPX4). Small interfering RNA (siRNA)-based RNA interference (RNAi) can precisely target any gene. However, achieving effective siRNA delivery is highly challenging. Here, we fabricated a TME-responsive metal-organic framework (MOF)-based biomimetic nanosystem (mFeP@si) with siGPX4 delivery and sonodynamic therapy (SDT) to treat OS by targeting ferroptosis. Under ultrasound (US) irradiation, mFeP@si achieves lysosomal escape via singlet oxygen (¹O₂)-mediated lysosomal membrane disruption and then accelerates ROS generation and glutathione (GSH) depletion. Meanwhile, siGPX4 silences GPX4 expression by binding to GPX4 mRNA and leads to the accumulation of toxic phospholipid hydroperoxides (PL-OOH), further magnifying the ROS storm and triggering ferroptosis. Notably, synergistic therapy remarkably enhances antitumor effects, improves the immunosuppressive TME by inducing potent immunogenic cell death (ICD), and increases the sensitivity of chemotherapy-resistant OS cells to cisplatin. Overall, this novel nanosystem, which targets ferroptosis by integrating RNAi and SDT, exhibits strong antitumor effects both in vitro and in vivo, providing new insights for treating OS.

1. Introduction

Osteosarcoma (OS) is the most common primary bone malignancy in children and adolescents and originates from malignant mesenchymal cells [1]. The current treatments for osteosarcoma mainly rely on pre-operative plus postoperative polychemotherapy and surgical reconstruction techniques, and chemotherapy regimens still depend on drugs similar to those used in the early 1980s [2]; moreover, survival rates have not improved during the past three decades [3]. Therefore, novel

treatments are urgently needed to obtain better outcomes.

Ferroptosis is a new type of regulated cell death characterized by iron accumulation, lethal lipid peroxidation, and GSH deprivation [4]. Ferroptosis has generated tremendous interest in tumor treatments, particularly in therapy-refractory tumors such as OS. A subset of tumors is sensitive to ferroptosis, and inducing ferroptosis in these tumors provides opportunities for tumor treatment [5]. Mechanistically, tumor cells, which are in a mesenchymal state and susceptible to metastasis, are sensitive to ferroptosis due to their unique metabolic characteristics,

* Corresponding author. Department of Spine Surgery and Musculoskeletal Tumor, Zhongnan Hospital of Wuhan University, 168 Donghu Street, Wuchang District, Wuhan, 430071, Hubei, China.

** Corresponding author. Department of Spine Surgery and Musculoskeletal Tumor, Zhongnan Hospital of Wuhan University, 168 Donghu Street, Wuchang District, Wuhan, 430071, Hubei, China.

*** Corresponding author. Department of Spine Surgery and Musculoskeletal Tumor, Zhongnan Hospital of Wuhan University, 168 Donghu Street, Wuchang District, Wuhan, 430071, Hubei, China.

E-mail addresses: renxiong.wei@whu.edu.cn (R. Wei), yanfeifei0120@whu.edu.cn (F. Yan), orthopedics@whu.edu.cn (L. Cai).

¹ These authors have contributed equally to this work.

<https://doi.org/10.1016/j.mtbio.2024.101053>

Received 30 January 2024; Received in revised form 27 March 2024; Accepted 9 April 2024

Available online 10 April 2024

2590-0064/© 2024 The Authors. Published by Elsevier Ltd. This is an open access article under the CC BY-NC license (<http://creativecommons.org/licenses/by-nc/4.0/>).

such as high levels of lipid peroxide and elevated unstable iron pools [6].

GSH/GPX4 is an important antioxidant system for regulating ferroptosis. GPX4 can eliminate ROS by degrading reduced GSH to oxidized glutathione (GSSG) [7]; more importantly, GPX4 is the only known enzyme that disrupts the lipid peroxidation chain reaction by using GSH as an electron donor to reduce toxic phospholipid hydroperoxides (PL-OOH) into their matching nontoxic phospholipid alcohols (PL-OH) and leaving GSSG [8]. Therefore, targeting GPX4 in OS cells to induce ferroptosis seems to be a promising therapeutic approach. For example, Xu et al. reported that microRNA-1287-5p inhibited the expression of GPX4 via RNAi and further promoted ferroptosis in OS [9].

RNA interference (RNAi) can precisely target any genetic locus involved in tumor progression and regulate the expression of relevant proteins. In particular, genes, which are thought to be undruggable using traditional approaches, have become druggable via RNAi therapy [10]. The approval of two siRNA drugs by the FDA indicates that RNAi therapy has entered a new era and holds great potential for the treatment of tumors [11,12]. However, despite these successful cases, achieving effective delivery of siRNA to the tissue of interest in vivo is still a challenge, especially for extrahepatic delivery.

As a noninvasive treatment, sonodynamic therapy (SDT) has more profound tissue permeability than photodynamic therapy (PDT) and is more suitable for deep tumors such as OS. By combining the synergetic effects of an acoustic sensitizer, US, and oxygen (O_2), SDT selectively kills tumor cells by producing a lethal dose of ROS [13]. Recent evidence indicates that synergistic therapy with SDT and RNAi has promising therapeutic effects on tumors [14]. Nevertheless, certain conditions, such as hypoxia and high GSH in the solid tumor TME, can limit the therapeutic efficacy of SDT [15]. Therefore, there is an urgent need to develop an acoustic sensitizer with self-produced O_2 and siRNA delivery to treat OS.

Metal-organic frameworks (MOFs) are burgeoning porous materials composed of metal ions and organic ligands with several intrinsic properties, such as good biocompatibility, high cargo loading capacity, and tailorable composition and structure. More interestingly, the coordination bonds between metal ions and organic ligands are sensitive to external pH, such as the acidic TME, making MOFs particularly suitable for regulated delivery of loaded drugs and tumor therapy [16]. Zirconium-based MOFs have been favored by researchers for their good thermodynamic stability, favorable biocompatibility, and low toxicity. Interestingly, Zr^{4+} has a high valence positive charge and a small radius, thus forming a strong coordination bond with the carboxyl group, which makes it easy to form chemically stable MOFs materials [17,18]. MOFs with porphyrins and porphyrin analogs (such as H_2TCPP) as organic ligands have gained increasing attention in the field of SDT [19]. In addition, H_2TCPP also has fluorescent properties and can be used for tracing and imaging. Recent studies have indicated that MOFs exhibit a strong combining capacity for siRNA through electrostatic attraction and multiple coordination bonds, and display great potential in siRNA delivery. For example, Zhuang et al. developed a ZIF-8 MOF and successfully delivered siRNA to breast cancer cells [20]. Guo et al. designed a MOF loaded with anti-TNF- α siRNA to achieve targeted siRNA delivery for treating rheumatoid arthritis [21]. Despite their great potential, nanoscale iron porphyrinic-based MOFs with siRNA delivery, SDT, and fluorescence properties have rarely been reported. Moreover, these studies on how siRNAs achieve lysosomal escape are superficial. Tumor cells exhibit a remarkable ability to bind homologous membrane proteins, making tumor-targeted drug delivery possible using membrane-coated nanodrugs [22]. Thus, tumor cell membranes are extracted to create biomimetic nanosystems [23].

In this work, a TME-responsive MOF-based biomimetic nanosystem (designated as mFeP@si) with siGPX4 delivery and SDT was conceptualized and fabricated to treat OS. Our synthesized iron porphyrin-based MOF (FePCN) can highly efficiently load siRNA for lysosomal escape and intracellular release, with an in vitro knockdown efficiency of more than 85% in 143B and K7M2 cells. Under US irradiation, FePCN decomposes

H_2O_2 to produce O_2 , which overcomes hypoxia and enhances SDT. As large amounts of ROS are produced, GSH is compensatorily depleted, and GSH depletion in turn inactivates GPX4 to some extent [24,25]. Furthermore, successful FePCN-mediated delivery of siGPX4 inactivates GPX4 and amplifies ROS storm, resulting in the accumulation of cytotoxic PL-OOH and ultimately killing OS cells by initiating ferroptosis. The synergistic therapy of SDT and RNAi also effectively promotes ICD to improve the immunosuppressive TME and increase the sensitivity of chemotherapy-resistant OS cells to cisplatin. Overall, our work constructed a TME-responsive nanosystem with siRNA delivery, SDT, and tumor targeting that can effectively overcome the challenges of RNAi delivery and the limitations of SDT, and provides new ideas for MOF-based RNAi and SDT synergistic therapy for treating OS.

2. Materials and methods

2.1. Materials

Zirconium oxychloride octahydrate ($ZrOCl_2 \cdot 8H_2O$), methyl p-formyl benzoate ($HCO_6H_4CO_2CH_3$), and pyrrole (C_4H_5N) were purchased from Merck (Germany). Hydrochloric acid (HCl), methanol (CH_3OH), propionic acid (CH_3CH_2COOH), ferrous chloride ($FeCl_2$), THF, and dimethylformamide (DMF) were purchased from Sinopharm Chemical Reagent Co. (Shanghai, China). The Calcein/PI Cell Viability/Cytotoxicity Assay Kit, LysoTracker Green, Reactive Oxygen Species Assay Kit, Mitochondrial Membrane Potential Assay Kit with JC-1, and Membrane and Cytosolic Protein Extraction Kit were purchased from Beyotime (Shanghai, China). A reduced GSH assay kit was purchased from Jiancheng Bioengineering Institute (Nanjing, China). An Intracellular Iron Colorimetric Assay Kit and MDA Assay Kit were obtained from Appligen (Beijing, China). The CCK-8 assay was purchased from Meilunbio (Dalian, China). Cisplatin was purchased from MedChemExpress (Shanghai, China). siGPX4 of human and mouse were purchased from Tsingke Biotech (Beijing, China). Lipomaster3000 was obtained from Vazyme (Beijing, China). The 143B, K7M2, 293T, and L929 cell lines were obtained from the Institute of Biochemistry and Cell Biology of the Chinese Academy of Sciences (Shanghai, China). Dulbecco's modified Eagle's medium (DMEM) and Roswell Park Memorial Institute (RPMI) were purchased from Hyclone (USA). Fetal bovine serum (FBS) was purchased from Gibco (USA). Penicillin-Streptomycin solution and Trypsin-EDTA solution were purchased from Biosharp (Beijing, China). A Milli-Q cycle purification system (Millipore, USA) was used to purify the water used in all experiments.

2.2. Synthesis of FePCN and FeP@si

Synthesis of FePCN: Iron porphyrin [5,10,15,20-tetrakis (4-carboxyphenyl) porphyrin]-iron (III) chloride (TCPP(Fe)) monomer, tetrakis (4-carboxyphenyl) porphyrin (H_2TCPP) monomer, and FePCN were prepared according to previous methods, with some modifications to the dosage and materials [26]. Briefly, for the FePCN NPs, $ZrOCl_2 \cdot 8H_2O$ (108.6 mg), TCPP(Fe) (7 mg), H_2TCPP (24 mg) and CF_3COOH (0.45 mL) were dissolved in 10 mL of DMF under US in a 20 ml Pyrex vial. The mixture was further heated at 120 °C for 18 h in an oven. After cooling to room temperature, the dark brown product at the bottom of the centrifuge tube was collected by centrifugation and washed with DMF three times and acetone twice. Finally, FePCN was dispersed in DMF (1 mg/mL) and stored at 4 °C.

Synthesis of FeP@si: The siRNA sequences used to knock down GPX4 in the human OS cell line 143B and mouse OS cell line K7M2 were 5'-GGA AGU GGA UGA AGA UCC AdTdT-3' and 3'dTdTU GGA UCU UCA UCC ACU UCC-5' and 5'-CTA TCT CTA GCT AGC CCT AdTdT-3'/5'-TAG GGC TAG CTA GAG ATA GdTdT-3' [27], respectively. The amount of siGPX4 used was in accordance with the optimized and recommended transfection concentration (at least 200 pmol per well in six-well plates, 8 μ L of 25 μ M siRNA added to 2 mL of medium) for cell experiments and

the recommended dosage (1.3 μg per mouse, 4 μL of 25 μM) for animal experiments [28]. According to the manufacturer's instructions, 1 OD of double-stranded RNA, with a mass of approximately 33 μg (2.5 nmol), was present at a concentration of 0.33 $\mu\text{g}/\mu\text{L}$ (25 μM) after adding 100 μL of DEPC-treated water. Thus, when calculating the dose of mFeP@si administered in vivo, the siRNA mass was consistent with the recommended dose of 1.3 μg . For the most efficient loading of siRNA, the volume ratio of FePCN (1 mg/mL) to siRNA (25 μM) was maintained at 4:1. The mass of FePCN in other groups, were consistent with the mass of FePCN in mFeP@si. The DMF solvent was removed by centrifugation at 11 000 rpm for 10 min, the FePCN was then washed three times with DEPC-treated water to completely remove DMF, and finally a solution of 1 mg/mL was prepared with DEPC-treated water. Subsequently, 5 μL , 10 μL , 15 μL , 20 μL , 40 μL , and 80 μL of 1 mg/mL FePCN were mixed with 20 μL of 25 μM siRNA solution, respectively, and dispersed under sonication for 30 min to obtain different volume ratios of FeP@si. NanodropOne was used to determine the free siRNA concentration in the supernatant after centrifugation at 5000 rpm for 5 min. Binding efficiency = (primary siRNA concentration - free siRNA concentration in the supernatant)/primary siRNA concentration \times 100 %.

2.3. Preparation of cell membranes and mFeP@si

Preparation of cell membranes: OS cell membranes were extracted using the Membrane and Cytosol Protein Extraction Kit (Beyotime, China) according to the manufacturer's instructions. In brief, 143B and K7M2 cells were selected for cell membrane extraction. Two OS cell lines were cultured in 15-cm dishes, and after they had grown to 85 % ~95 % confluence, the culture medium was discarded, and the cells were washed with PBS. A cell scraper was used to scrape the OS cells, and the cells were collected by centrifugation. The cell precipitates were washed with ice-cold PBS and subsequently centrifuged, after which the supernatant was discarded as much as possible. Then, the cells were resuspended in 1 ml of Solution A supplemented with phenyl methyl sulfonyl fluoride (PMSF) and incubated in an ice bath for 10–15 min. Afterward, the cells were freeze-thawed with liquid nitrogen several times until they were lysed. The mixture was centrifuged at 700 \times g for 10 min at 4 $^{\circ}\text{C}$, the supernatant was carefully transferred to another centrifuge tube and centrifuged at 14 000 \times g for 30 min at 4 $^{\circ}\text{C}$, and the precipitate contained the cell membrane fragments.

Preparation of mFeP@si: 143B and K7M2 cell membrane solids (10 mg) were dispersed in 10 mL of DEPC-treated water by US. Sequentially, the two prepared cell membranes and FeP@si (1 mg/mL) were mixed and dispersed, respectively. Finally, the two mixtures were extruded through a liposome extruder (Changsha Nanoapparatus Co., Limited) with a polycarbonate porous membrane (20 μm) to obtain 143B-mFeP@si and K7M2-mFeP@si, respectively. Cell membrane-coated FePCN (mFePCN) was prepared via the same methods as those described above. Unless otherwise stated, the concentration of mFeP@si and FeP@si was based on the amount of FePCN.

2.4. Characterization of FePCN and mFeP@si

Transmission electron microscopy (JEM-F200, Japan) and an accompanying energy spectrometer were used to observe the microstructure and elemental distribution of FePCN. XPert Pro instrument (The Netherlands) was used to analyze all powder X-ray diffraction (XRD) data. Fourier transform infrared spectrum analyzer (FT-IR5700, USA) was utilized for FT-IR spectroscopy. A UV spectrophotometer (UV-2600, Shimadzu, Japan) was used to obtain UV-visible absorption spectra. A Leica STELLARIS 5 SR (Leica, Germany) was used to acquire confocal laser fluorescence microscopy (CLSM) images. A flow cytometer (FCM, cytoFlex S, Beckman) was used to analyze the FCM data. Cell viability was assessed by a CCK-8 assay with a microplate reader (VICTOR Nivo, PerkinElmer) at 450 nm. In vivo, an animal imaging system (IVIS Lumina XRMS, PerkinElmer, USA) was utilized for

fluorescence imaging.

2.5. Enzyme-like activities of FePCN

Detection of O_2 : To investigate the CAT-like activity of FePCN, equal volumes of FePCN (40 $\mu\text{g}/\text{mL}$) and H_2O_2 (10 mM) were mixed at room temperature. The dissolved O_2 concentration in the water was measured with time by a JPB-609L portable dissolved oxygen meter (REX Instruments, Shanghai).

Detection of $^1\text{O}_2$: To investigate the peroxidase-like activity of FePCN, equal volumes of FePCN (40 $\mu\text{g}/\text{mL}$) and the DPBF Assay Probe (20 $\mu\text{g}/\text{mL}$) were mixed in the dark. DPBF aqueous solution (10 $\mu\text{g}/\text{mL}$) was added as a control. Every 1 min, the solution was irradiated with or without US irradiation (1 W/cm^2), and the absorption peak at 415 nm was detected by UV-visible spectroscopy for 15 min.

2.6. Cell transfection and RT-qPCR

When the density of 143B and K7M2 cells reached 70 %, siRNA transfection was performed according to the manufacturer's instructions. Briefly, 8 μL of 25 μM siRNA and 5 μL of Lipomaster3000 were added to 125 μL of Opti-MEM, respectively, and then mixed. After 15 min, the mixed solution was added dropwise to a 6-well plate. At 48 h, TRIzol reagent was used to extract total RNA, which was then reverse transcribed to cDNA with a PrimeScript RT kit. Finally, gene expression was assessed with SYBR green PCR mix. The sequences of primers used were as follows: human GPX4: forward, 5'-GAG GCA AGA CCG AAG TAA ACT AC-3'; human GPX4: reverse, 5'-CCG AAC TGG TTA CAC GGG AA-3'; human GAPDH: forward, 5'-TGG TAT CGT GGA AGG ACT C-3'; human GAPDH: reverse, 5'-AGT AGA GGC AGG GAT GAT G-3'; mouse GPX4: forward, 5'-GCC TGG ATA AGT ACA GGG GTT-3'; mouse GPX4: reverse, 5'-CAT GCA GAT CGA CTA GCT GAG-3'; mouse GAPDH: forward, 5'-ATC ATC CCT GCA TCC ACT-3'; and mouse GAPDH: reverse, 5'-ATC CAC GAC GGA CAC ATT-3'.

2.7. Cell uptake of NPs

For fluorescence observations, two OS cell lines were inoculated in confocal dishes at a density of 5×10^4 cells/dish, and 40 μL of FePCN (1 mg/mL) or mFePCN (1 mg/mL) was added to bring the final concentration of NPs to 20 $\mu\text{g}/\text{mL}$ after the cell density reached 70%–80 %. At 0, 1, 2, 4, and 6 h after incubation with FePCN or mFePCN, the nuclei were stained with DAPI after fixation with 4 % paraformaldehyde and observed by CLSM. In parallel experiments, FCM was used to assess the uptake of mFePCN by 143B cells. To investigate whether FePCN can effectively carry siRNA, we used FAM-labeled siRNA to evaluate the intracellular distribution of FePCN (red fluorescence) and siRNA (green fluorescence). After incubation for 6 h, the nuclei were stained with DAPI after fixation with 4 % paraformaldehyde, and the cells were observed by CLSM.

2.8. Study of the colocalization of NPs and lysosomal escape

143B and K7M2 cells were seeded in confocal dishes at a density of 5×10^4 cells per dish. mFeP@si (final concentration: 20 $\mu\text{g}/\text{mL}$) was added after the cells reached 70%–80 % confluence. After incubating for 6 h, one group was ultrasonicated (1 w/cm^2 , 1 min), and the other group not subjected to irradiation served as a control. After another 4 h, all the cells were washed with PBS, the culture medium was replaced with fresh medium containing LysoTracker Green (50 nM), and the samples were incubated at 37 $^{\circ}\text{C}$. After 30 min, the culture medium was removed, and the cells were washed with PBS. Hoechst 33342 (Biosharp, China) was used to stain the nucleus. Images were observed by confocal microscopy (LysoTracker Green: Ex/Em = 535/617 nm).

2.9. Cell viability assays

In brief, 293T and L929 cells were seeded in 96-well plates (3×10^3 cells/well) with different concentrations of mFeP@si and incubated at 37 °C in a humidified incubator containing 5 % CO₂. After 24 h, 100 µl of culture medium containing 10 µL of CCK-8 solution was added to each well and incubated for another hour. The optical absorbance of each well was read at 450 nm using a microplate reader.

2.10. Antitumor effect of mFeP@si in vitro

Live and dead cell staining: Briefly, 143B and K7M2 cells were divided into 6 groups (G1: control; G2: naked-si (8 µL, 25 µM); G3: mFePCN (40 µL, 1 mg/mL); G4: mFeP@si (40 µL, 1 mg/mL); G5: US + mFePCN (40 µL, 1 mg/mL); and G6: US + mFeP@si (40 µL, 1 mg/mL)) and inoculated in 6-well plates (2×10^5 cells/well) for 24 h. Then, the cells were washed with PBS, and the supernatants were replaced with fresh complete DMEM/1640 with or without different NPs (final concentration: 20 µg/mL) and incubated for another 6 h, followed by sonication. For the groups (G5 and G6) exposed to US irradiation, a sonicator device purchased from Shenzhen WELLD Medical Electronics Company (Shenzhen, China) was utilized. The intensity of the US irradiation was 1.0 W/cm² (frequency: 1 MHz; duty cycle: 50 %) for 1 min. Twelve hours after US irradiation, the number of live and dead cells was measured by the Calcein/PI Cell Viability/Cytotoxicity Assay Kit (Beyotime, China) according to the manufacturer's protocol. Images of live and dead cells were captured using a fluorescence microscope (calcein AM: Ex/Em = 494/517 nm; PI: Ex/Em = 535/617 nm).

Colony formation assay: Briefly, 143B and K7M2 cells were inoculated in 6-well plates (1000 cells/well) and treated every two days as described above. On day 7, the cells were fixed with 4 % paraformaldehyde and stained with crystal violet. Images were captured with a digital camera.

2.11. ROS generation

Briefly, 143B and K7M2 cells were divided into 6 groups, inoculated into 6-well plates (2×10^5 cells/well) for 24 h, incubated with NPs for 6 h, and then subjected to US irradiation as described above. Six hours after US irradiation, Opti-MEM was used to dilute DCFH-DA to 10 µM. The medium was replaced with Opti-MEM staining solution, and the cells were incubated for another 20 min at 37 °C. The fluorescence images were captured under a fluorescence microscope. In parallel experiments, 6 h after US irradiation, the cells were incubated with 10 µM DCFH-DA in Opti-MEM for 20 min. The cells were subsequently digested and resuspended in PBS, after which the ROS levels were quantified via FCM (Beckman, USA). The green fluorescence of DCFH-DA was determined at Ex 488 nm and Em 525 nm.

2.12. Mitochondrial membrane potential determination

A mitochondrial membrane potential assay kit with JC-1 (Beyotime, China) was used to assess MMP loss according to the manufacturer's protocol. In brief, OS cells were divided into the 6 groups mentioned above. 143B and K7M2 cells were seeded in confocal dishes (5×10^4 cells/dish), cultured for 24 h and treated as described above. JC-1 working solutions were prepared according to the manufacturer's protocol, and the cells were incubated at 37 °C for 20 min. Then, the cells were washed twice with precooled staining buffer, and 2 mL of fresh medium was added. Confocal images were obtained by CLSM. In parallel experiments, the cells were digested and suspended after incubation with JC-1 working solution for analysis via FCM (J-aggregates: Ex/Em = 585/590 nm; J-monomer: Ex/Em = 514/529 nm).

2.13. Intracellular GPX4 expression

In brief, OS cells were divided into the 6 groups mentioned above. 143B and K7M2 cells were seeded in confocal dishes (5×10^4 cells/dish), cultured for 24 h and treated as described above. Twelve hours after US irradiation, 143B and K7M2 cells were fixed with 4 % paraformaldehyde, blocked with goat serum, and lysed with Triton X-100. After incubation with a GPX4 primary antibody (1:200) overnight and a Cy3-labeled secondary antibody (1:200) for 1 h in the dark, the cells were observed via CLSM (Cy3: Ex/Em = 550/570 nm).

2.14. Evaluating ferroptosis in OS cells

Intracellular total iron: The iron ion concentration was analyzed using an Intracellular Iron Colorimetric Assay Kit according to the manufacturer's instructions. Briefly, the treated cells were lysed and centrifuged at 12 000 × rpm for 5 min to obtain the supernatant. 100 µL of the supernatant was incubated with 100 µL of solution A for 1 h at 60 °C. Then, 30 µL of test working solution was added, and the mixture was incubated for 30 min at RT. After centrifugation at 12 000 × rpm for 5 min, 100 µL of the supernatant was added to a 96-well plate, and the optical absorbance of each well was read at 550 nm using a microplate reader. The relative iron content is expressed as the ratio of the absorbance values of the treated and control cells.

Lipid peroxidation assessment: A Lipid Peroxidation MDA Assay Kit was used to detect lipid peroxidation (LPO) levels. According to the manufacturer's protocol, after washing with PBS, lysis buffer was added to the cells, the cells were homogenized on ice, the mixtures were centrifuged at 10 000 × g for 10 min at 4 °C, and the supernatant was subsequently collected. 100 µL of each supernatant was incubated with 100 µL of the test work solution for 15 min at 100 °C and then cooled to RT. The mixtures were centrifuged at 10 000 × g for 10 min to obtain supernatants, and the absorbance was read at 535 nm using a microplate reader. The relative MDA content is expressed as the ratio of the absorbance values of the treated and control cells.

Intracellular GSH concentration: A reduced glutathione (GSH) assay kit was used to measure the GSH concentration in the cells. Briefly, after being washed and lysed, 0.1 mL of cell suspension and 0.1 mL of Reagent I were mixed adequately and centrifuged at 3500 × rpm for 10 min to obtain the supernatant. Then, 100 µL of Reagent II and 25 µL of Reagent III were added to 100 µL of supernatant and mixed with slight shaking. The absorbance of each well was measured at 405 nm using a microplate reader. The relative GSH concentration is expressed as the ratio of the absorbance values of treated and control cells.

2.15. Immunogenic cell death (ICD) of OS cells

Detection of the secreted ATP concentration: An ATP Assay Kit was used to detect the secreted ATP concentration in the medium. Briefly, the cell culture media of 143B and K7M2 cells subjected to different treatments were collected and centrifuged at 5000 rpm for 10 min to obtain the supernatants. Then, 100 µL of test working solution was added to the 96-well plate, and after 5 min, 20 µL of the supernatant was added and quickly mixed. The RLU value was determined by a luminometer.

Evaluation of CRT and HMGB1 expression: 143B and K7M2 cells were inoculated in confocal dishes (5×10^4 cells/dish) and incubated for 24 h. After the treatments mentioned above, 4 % paraformaldehyde, TRITON (0.3 %), and goat serum (Boster, China) were added in order. After removing the goat serum, calreticulin (CRT) and high mobility group b1 protein (HMGB1) primary antibodies were added at a dilution of 1:400 in PBS and incubated overnight at 4 °C. After washing three times with PBS, goat anti-rabbit IgG was added at a dilution of 1:200 in PBS, and the samples were incubated at 37 °C for 1 h in the dark. Nuclei were stained with DAPI for 5 min, after which the cells were observed via CLSM (Cy3: Ex/Em = 550/570 nm).

2.16. Effects on cisplatin-resistant OS *in vitro*

In parallel experiments, we replaced 143B cells with cisplatin-resistant 143B cells (143B-R). *In vitro* live/dead cell staining and colony formation assays, as described above, were used to investigate whether synergistic treatment with SDT and RNAi is effective for treating cisplatin-resistant osteosarcoma cells.

2.17. *In vivo* distribution

All animal experimental procedures were authorized by the Animal Care and Use Committee of Zhongnan Hospital, Wuhan University (NO. ZN2023172) and were conducted following the Guidelines for the Care and Use of Laboratory Animals. Briefly, 4-week-old BALB/c male mice were subcutaneously injected with 5×10^6 K7M2 cells into the right flank to establish a subcutaneous OS model. Mice with a tumor volume of 100 mm^3 were selected and then randomized into different groups (3 mice in each group). Saline, FeP@si (siRNA: 1.3 μg per mouse) and mFeP@si (siRNA: 1.3 μg per mouse) were intravenously injected through the tail vein. Fluorescence images were obtained using a live imaging system (Ex = 561 nm, Em = 660 nm) at pre-treated time point (0 h, 2 h, 4 h, 6 h, 12 h and 24 h). Then, all animals were subjected to euthanasia at 48 h, and the major organs (including the heart, lung, liver, spleen, and kidney) and tumor tissues were separated and imaged in the same imaging system.

2.18. *In vivo* antitumor effects

To establish a subcutaneous OS model, we subcutaneously injected 5×10^6 143B cells into the right flank of the mice and measured the tumor size every 3 days. After 7 days, mice with a tumor volume of 100 mm^3 were selected and then randomized into the following six treatment groups (4 mice in each group): G1, saline; G2, naked-si (1.3 μg siRNA per mouse); G3, mFePCN (16 μg per mouse); G4, mFeP@si (16 μg per mouse); G5, US + mFePCN (16 μg per mouse); and G6, US + mFeP@si (16 μg per mouse). The mass of 4 μL of 25 μM siRNA was approximately 1.32 μg , which is in accordance with the recommended dosage for experimental animals (1.3 μg per mouse). Notably, to be consistent with the recommended siRNA usage in mouse and for sufficient SDT effects, for G4 and G6, 16 μL of 1 mg/mL FePCN and 4 μL of 25 μM siRNA (volume ratio 4:1) were used to construct the mFeP@si used in animal experiments and 20 μL of mFeP@si (800 $\mu\text{g}/\text{mL}$) contained 100 pmol siRNA.

To maintain a consistent siRNA quality, 16 μL of 1 mg/mL FePCN was used to load the siRNAs. The different drugs were injected into the tail vein every three days, and for the G5 and G6 groups, US (2.5 W/cm², 3 min) was applied 24 h after injection. The nude mice were anesthetized with isoflurane. Then, the ultrasonic coupling agent was added to a 2 cm deep tube, and the tumor was placed into the ultrasonic coupling agent for exact ultrasonic radiation. All groups were continuously treated for three weeks and sacrificed at 21 days. Whole blood was obtained from nude mice for serum biochemical analysis, and tumors and major organs were isolated and analyzed histologically (H&E, immunohistochemistry of GPX4 and Ki67, immunofluorescence of CRT, HMGB1, and TUNEL staining). The tumor volumes were calculated according to the following widely used formula: tumor volume (mm^3) = axial length (mm) \times (lateral axial length)² (mm^2)/2. We also recorded the weights of the nude mice throughout the experiment.

2.19. Biosafety assessment *in vivo*

On the last day of the treatment procedure, major organs (heart, liver, spleen, lung, and kidney) and fresh blood samples were collected from three mice in each group to evaluate the biosafety of the prepared NPs. H&E staining was used to assess the toxicity of NPs to organs, and blood samples were used to analyze serum biochemical indicators (ALT,

AST, and BUN) and blood parameters (WBC, RBC, and HB).

2.20. Statistical analysis

All the data are presented as the mean \pm standard deviation. Student's *t*-test was used to compare the mean values of unpaired data. Analysis of variance (ANOVA) was used to analyze the differences between multiple groups. GraphPad Prism version 8.30 software was used for the statistical analyses (GraphPad; La Jolla, CA). All the experiments were repeated three times. A *P* value < 0.05 was considered to indicate statistical significance (**p* < 0.05, ***p* < 0.01, ****p* < 0.001).

3. Results and discussion

3.1. Synthesis and characterization of FePCN, FeP@si and mFeP@si

RNA interference (RNAi) is attracting more and more attention because of its potential to precisely target any gene involved in tumor progression and regulate the expression of relevant proteins and genes that are considered undruggable using traditional methods have become druggable via RNAi [29]. However, *in vivo* delivery of siRNA remains an enormous challenge. It has been reported that there is strong electrostatic attraction between the metal nodes of MOFs and the backbone phosphates of the siRNA, and the porous structure can protect the siRNA and allow for efficient RNA loading. Thus, MOFs seem to be potential delivery vessels for siRNA. Here, we report a FePCN-based biomimetic nanosystem (designated as mFeP@si) with siGPX4 delivery, catalase (CAT)-like activity, peroxidase-like activity, fluorescent properties and enhanced SDT. The design and synthetic routes of mFeP@si are briefly outlined in Fig. 1A. To synthesize FePCN with CAT-like activity, peroxidase-like activity and fluorescent properties, tetrakis (4-carboxyphenyl) porphyrin iron (III) chloride (TCPP(Fe) monomer and tetrakis (4-carboxyphenyl) porphyrin (H₂TCPP) monomer were synthesized according to methods reported in the literature. FT-IR confirmed the successful synthesis of H₂TCPP and TCPP(Fe) (Figs. S1 and S2). Then, TCPP(Fe), H₂TCPP and Zr⁴⁺ were mixed in DMF and centrifuged to obtain FePCN via a one-pot method. Subsequently, in DEPC-treated water, siRNA was loaded into FePCN to obtain FeP@si. The final product, mFeP@si, was obtained by coating FeP@si with OS cell membranes.

Adequate characterizations of NPs are essential for therapeutic implications. TEM was used to characterize the micromorphology of FePCN (Fig. 1B), FeP@si (Fig. 1C), and mFeP@si (Fig. 1D). As shown in the TEM images, all the nanoparticles (NPs) exhibited a hollow nanorod-like structure with a uniform particle size, and neither the siRNA loading nor the membrane coating changed the micromorphology of the MOF. The linear streaks are visible on the surface of FePCN. Notably, the blurring of the linear streaks on the surface of the mFeP@si, as shown in Fig. 1D, demonstrated successful encapsulation of the cell membrane. To further characterize the encapsulating of OS cell membranes, we also extracted the cell membranes of OS cells and mFeP@si, and observed the distribution of specific membrane proteins by SDS-PAGE (sodium dodecyl sulfate–polyacrylamide gel electrophoresis). As shown in Fig. S3, the encapsulated cell membranes still have complete structures and retain almost all specific membrane proteins, which indicates that mFeP@si has excellent homologous targeting potential. HAADF (High-angle annular dark-field imaging) and elemental mapping were used to analyze the elemental composition of FePCN. As shown in Fig. 1E, C, N, O, Zr, and Fe were uniformly distributed in the aggregations and these images confirmed the successful synthesis of FePCN. EDS was adopted to further analyze the content of C, Zr, and Fe (Fig. 1F), and the result was consistent with the elemental mapping. XPS analysis was applied to further characterize the elemental composition of FePCN. To obtain a deeper understanding of the surface chemistry of FePCN, an XPS evaluation was also performed. The wide-scan XPS spectrum (Fig. S4A) clearly shows that FePCN is mainly composed of C, O, N, Zr and Fe. The high-resolution XPS spectra of Fe 2p after Gaussian curve fitting was

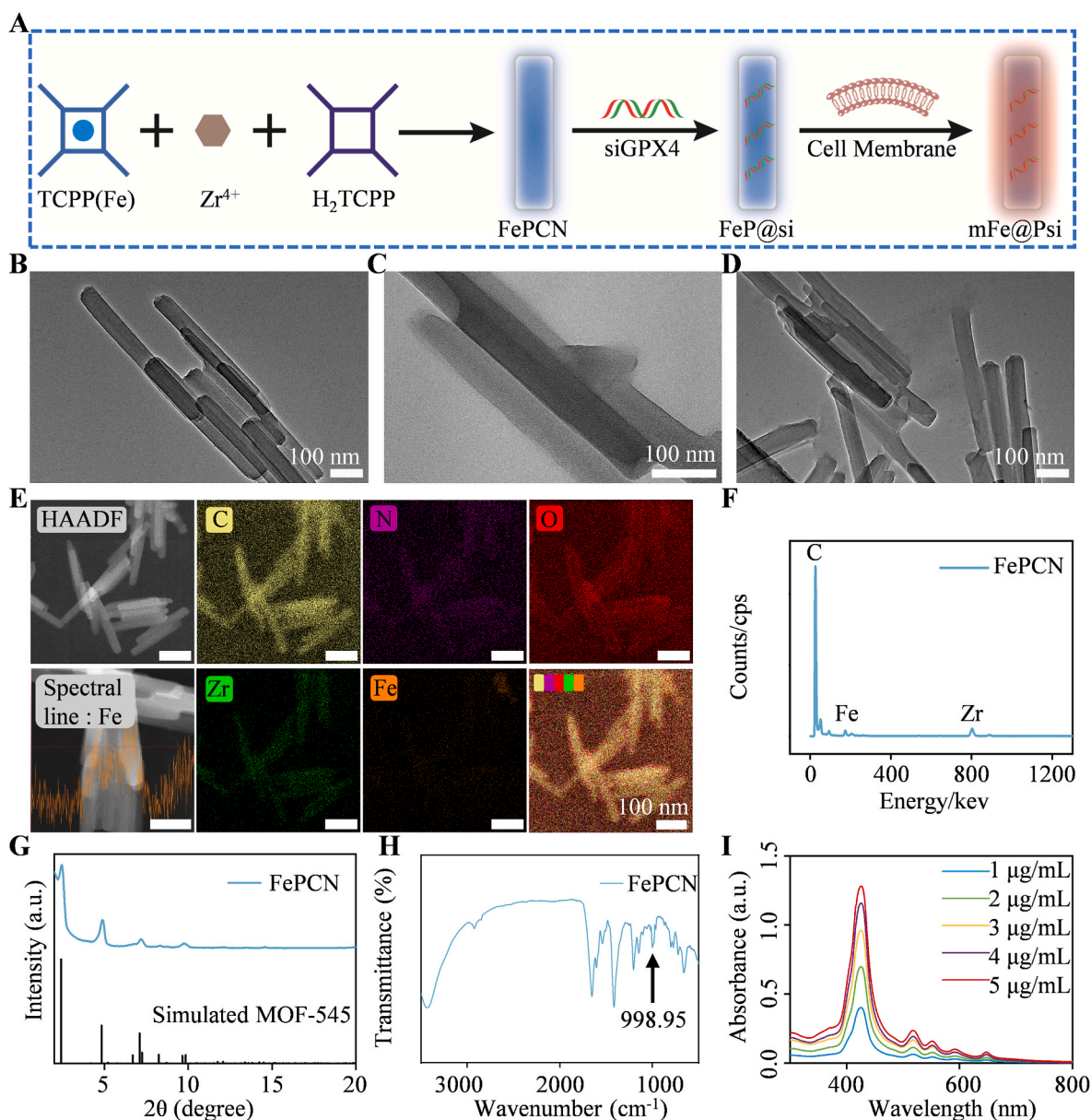


Fig. 1. A) Schematic of mFeP@si fabrication. B–D) TEM images of FePCN, FeP@si, and mFeP@si (Scale bar: 100 nm). E) HAADF and EDS mapping images of FePCN (Scale bar: 100 nm). F) C, Fe and Zr content in FePCN by EDS analysis. G) XRD and H) FT-IR characteristics of FePCN. I) UV–Vis spectra of different concentrations of FePCN.

adopted to examine the Fe component in detail. Fe 2p core level spectra of FePCN consists of six characteristic peaks (Fig. S4B). By calculating the area under each characteristic peak, the Fe³⁺ and Fe²⁺ accounted for 92 % and 8 %, respectively. XRD, FT-IR, and UV–visible absorption spectroscopy are commonly used to analyze the characteristic peaks of materials to further confirm successful synthesis. Notably, in the XRD pattern, the characteristic peaks of FePCN were consistent with those of the previously reported MOF-545, which proves the successful synthesis of the classical MOF (Fig. 1G). The successful doping of Fe in FePCN was confirmed by the Fe–N stretching vibration peak at 998.95 cm⁻¹ in the FT-IR spectrum (Fig. 1H). UV–Vis absorption spectroscopy of FePCN proved that FePCN remained stable at different concentrations (Fig. 1I). Moreover, the successful synthesis of FeP@si was confirmed by UV–Vis absorption spectroscopy, as shown in Fig. 2A. As simple and reproducible tools for investigating the size and surface charge of particles, dynamic light scattering (DLS) and zeta potential (ZP) methods are widely utilized. The ZP of FePCN, FeP@si, and mFeP@si were 35.80 ± 0.66

mV, −8.56 ± 1.22 mV, and −33.60 ± 0.70 mV, respectively (Fig. 2B). siRNA binding changed the ZP of FePCN from positive to negative, which might be attributed to the phosphate backbone of the siRNA. These findings demonstrated that FePCN has a good loading capacity for siRNAs. The wrapping of the cell membrane further decreased the zeta potential of mFeP@si. As shown in Fig. 2B, DLS results suggest that FePCN, FeP@si, and mFeP@si have homogeneous hydrodynamic diameters and the average particle size of FePCN, FeP@si, and mFeP@si are 482.6 ± 3.8 nm, 462.5 ± 7.0 nm, and 491.8 ± 7.5 nm, respectively, which is consistent with the TEM results. To simulate the stability of the NPs during circulation in vivo, we tested the stability of mFeP@si in DMEM and DMEM+10 % FBS. As shown in Fig. S5, the hydrodynamic size of mFeP@si did not change significantly over 3 days. Notably, the hydrodynamic diameter of mFeP@si increased slightly in the two media compared to the hydrodynamic size in water, which may be related to the complex composition of the medium. Notably, this increase in particle size may be due to the adsorption of amino acids and proteins in the

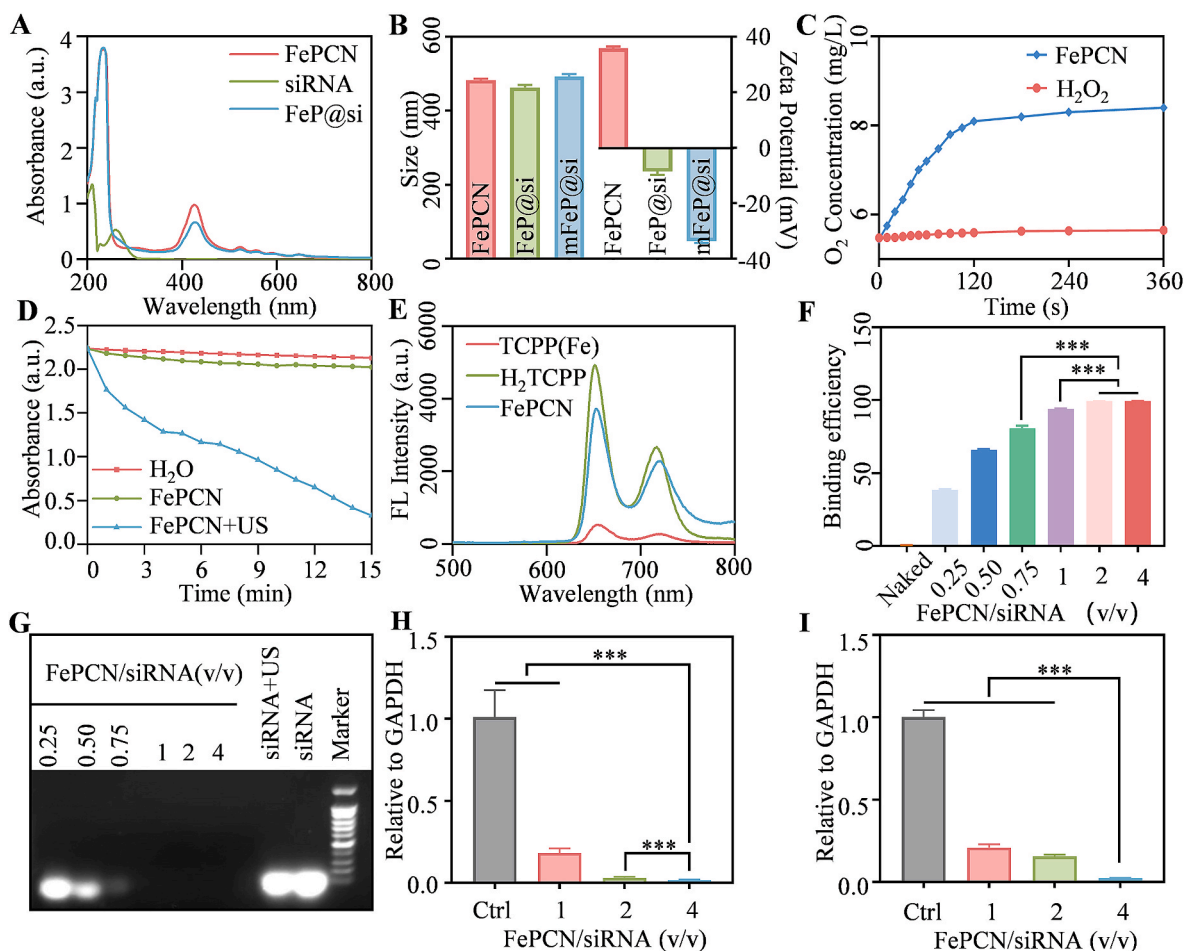


Fig. 2. A) UV-Vis spectra of FePCN, siRNA, and FeP@si. B) zeta potential and hydrodynamic diameter of FePCN, FeP@si, and mFeP@si. C) The capacity of FePCN to decompose H_2O_2 to produce O_2 . D) The capacity of FePCN-mediated $^1\text{O}_2$ generation with/without US irradiation. E) Fluorescence properties of TCPP(Fe), H_2 TCPP, and FePCN. F) The binding efficiency of FePCN to siRNA at different volume ratios. G) Assessment the free siRNA in supernatant of FeP@si at different volume ratios by Agarose gel electrophoresis (AGE). H) Evaluation the knockdown efficiency of mFeP@si at different volume ratios for GPX4 in 143B cells. I) Evaluation of the knockdown efficiency of mFeP@si at different volume ratios for GPX4 in K7M2 cells. (n = 3, ***p < 0.001).

FBS, rather than the mFeP@si itself becoming larger.

3.2. Enhanced SDT potential and siRNA binding efficiency

SDT has received increased attention since it is non-invasive and has deeper tissue penetration, making it more suitable for treating profound tumors. However, the microenvironment of solid tumors (such as hypoxia and high GSH levels) often limits the efficacy of SDT. High H_2O_2 levels in the TME can serve as a source of oxygen to alleviate hypoxia. To assess the CAT-like activity of FePCN, we tested the ability of FePCN to utilize H_2O_2 to produce O_2 under different conditions by a dissolved oxygen analyzer (JPB-609 L). As shown in Fig. 2C, FePCN can decompose H_2O_2 to produce O_2 , which indicates that FePCN has excellent CAT-like activity and is expected to improve hypoxia and enhance SDT. Achieving lysosomal escape of siRNA payloads is one of the major barriers for siRNA delivery in vivo and is the basis for targeting and degrading specific mRNAs in the cytoplasm [30]. Cytotoxic singlet oxygen ($^1\text{O}_2$) can disrupt the membrane of lysosomes and enable the delivery of loaded drugs into the cytoplasm, thus achieving lysosomal escape of the NPs [31]. Therefore, we next assessed the effect of SDT on the peroxidase-like activity of FePCN by detecting the $^1\text{O}_2$ concentration with the probe 1,3-diphenylisobenzofuran (DPBF). As shown in Fig. 2D, under the synergistic effect of US and FePCN, the absorption curve of DPBF decreased significantly with time. This suggests that under US irradiation, FePCN produces a large amount of $^1\text{O}_2$, which ensures

lysosomal escape and the effects of SDT. Electron spin resonance (ESR) was used to further examine the capacity of FePCN to produce $^1\text{O}_2$ under ultrasonic irradiation. As shown in Fig. S6, there are three peaks from left to right with the last peak being slightly lower than the first two. This result is consistent with the characterization of the $^1\text{O}_2$ ESR spectrogram and proves the production of $^1\text{O}_2$ by SDT. In brief, Under US irradiation, FePCN achieved tandem catalysis from H_2O_2 to O_2 and from O_2 to $^1\text{O}_2$, suggesting its potential to improve tumor hypoxia, achieve lysosomal escape and enhance SDT. In addition, to further evaluate the Fenton reaction and chemo-dynamic therapy (CDT) effects, we also detected hydroxyl radicals ($\cdot\text{OH}$) by ESR. There are four peaks in the ESR spectrogram and the ratio of the peaks from left to right is approximately 1:2:2:1 (Fig. S7). This is consistent with the hydroxyl radical characterization and suggests the occurrence of a Fenton reaction and CDT effects. Due to their fluorescent properties, NPs are often used for tracing and imaging. Therefore, we examined the fluorescence properties of FePCN. As shown in Fig. 2E, the fluorescence properties of FePCN were similar to those of H_2 TCPP.

The regulation of ferroptosis is strongly related to GSH biosynthesis and the normal function of GPX4, and GPX4 is paramount to this metabolic axis [32]. Therefore, inhibiting GPX4 expression to induce ferroptosis is a feasible strategy for OS therapy. Next, we synthesized human and mouse siGPX4s and negative control siRNA (si-NC) according to previous methods [27]. The siRNAs were transfected into 143B and K7M2 cells for 48 h, respectively. RT-qPCR was performed to detect

the knockdown efficiency of GPX4 and to determine the siRNA sequences to be used for subsequent experiments. As shown in Figs. S8 and S9, the second siGPX4 of human origin and the second siGPX4 of mouse origin had knockdown efficiencies greater than 90 % and 80 % in 143B and K7M2 cells, respectively, and were therefore selected for subsequent experiments. To investigate the loading ability of FePCN on siRNA, we explored the influence of the volume ratio (FePCN/siGPX4) on the binding efficiency at a specific concentration (FePCN: 1 mg/mL, siGPX4: 25 μ M). As shown in Fig. 2F, when the volume ratio reached 2 or higher, almost all siRNAs were bound to FePCN, which indicated that FePCN had a good loading capacity for siRNAs. When the volume ratio reached

2 or higher, no siRNA bands were shown in the agarose gel electrophoresis experiments, indicating that almost no free siRNA was present in the solution (Fig. 2G). This result also confirms the binding efficiency in another way. In addition, US irradiation hardly caused the degradation of siRNAs. The electrostatic attraction and multiple coordination bonds between the siRNA phosphate backbone and the FePCN metal ions account for the strong binding ability of FePCN to siRNA [33]. Finally, mFeP@si with volume ratios of 1, 2 and 4 were used to assess the knockdown efficiency of GPX4 in 143B and K7M2 cells by RT-qPCR and the knockdown efficiency was maximized in both 143B and K7M2 cells when the volume ratio was 4 (Fig. 2H and I). To further evaluate

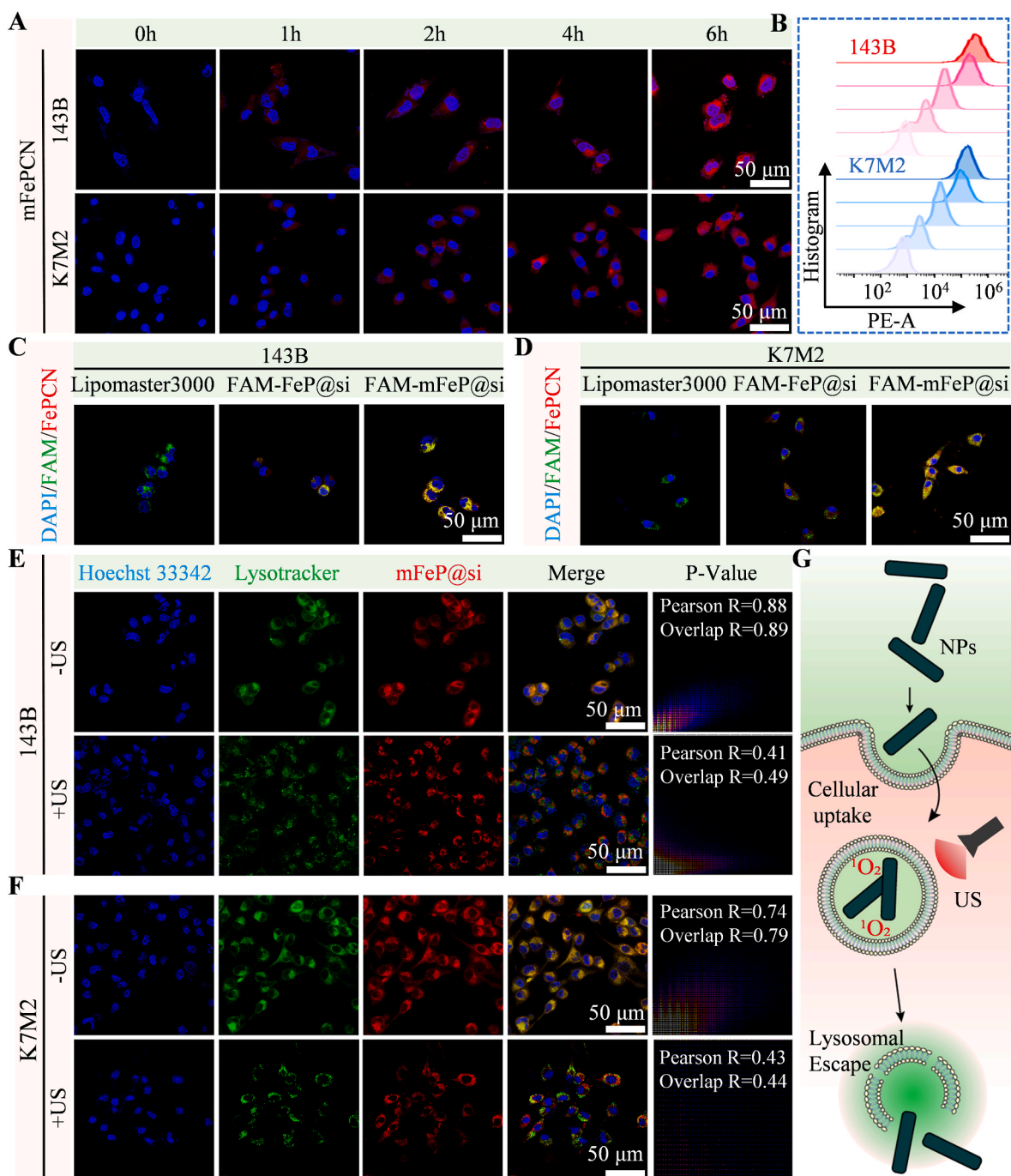


Fig. 3. A-B) Uptake of mFePCN by 143B and K7M2 at preset time points (0 h, 1 h, 2 h, 4 h, and 6 h) detected by CLSM and FCM (Scale bar: 50 μ m). C-D) Positional distribution of siRNA (green fluorescence) and FePCN (red fluorescence) in 143B and K7M2 cells assessed by CLSM (Scale bar: 50 μ m). E-F) Analysis of mFeP@si lysosomal escape and fluorescence co-localization with or without US irradiation in 143B and K7M2 cells (Scale bar: 50 μ m). G) Schematic illustration of 1O_2 -mediated lysosomal escape.

the knockdown efficiency of GPX4 on protein level, we extracted proteins from two OS cells after different treatments, and the Western Blot results showed that mFeP@si with a volume ratio of 4 most efficiently silenced the expression of GPX4 on protein level, and this result was consistent with RT-qPCR (Fig. S10). These results indicate that mFeP@si with a volume ratio of 4 efficiently silences GPX4 at both the mRNA and protein levels, with great potential to induce ferroptosis. Notably, to be consistent with the recommended siRNA usage of commercial transfection reagents and for sufficient SDT effects, for one well of a 6-well plate, 40 μL of 1 mg/mL FePCN and 10 μL of 25 μM siRNA (volume ratio 4:1) were used to construct the mFeP@si used in the following cell experiments and 50 μL of mFeP@si (800 $\mu\text{g}/\text{mL}$) contained 250 pmol siRNA.

3.3. Cellular uptake and lysosomal escape

Nanodrugs are favored by researchers because of their specific physicochemical, biological, and catalytic activities, which can overcome many of the limitations of conventional agents [34]. Remarkably, various factors, such as size, zeta potential, and surface modifications, influence the cellular uptake and intracellular transport of NPs and determine whether NPs are internalized through phagocytosis (such as bacteria and cargos of large sizes) or endocytosis (such as membrane fusion) [35]. Therefore, it is crucial to assess the cellular uptake of mFePCN prior to further experiments. We incubated mFePCN and FePCN with 143B and K7M2 cells, respectively, and evaluated the uptake efficiency of the two nanoparticles at predetermined time points (0 h, 1 h, 2 h, 4 h, and 6 h) by CLSM. The uptake of mFePCN by both 143B and K7M2 cells gradually increased with time and reached a maximum at 6 h, as evidenced by intracellular red fluorescence (Fig. 3A). For further confirmation, we assessed the efficiency of mFePCN uptake by OS cells at the same time points by FCM, and the results were consistent with those of CLSM (Fig. 3B). Tumor cell membranes can provide homologous targeting ability for NPs, which facilitates the aggregation and internalization of NPs at the tumor site [36]. Therefore, we analyzed the effect of OS cell membranes on FePCN internalization. As shown in Fig. S11, 143B cells showed significantly greater uptake of mFePCN than of FePCN. K7M2 cells demonstrated the same results (Fig. S12). These differences in cellular uptake may be related to the zeta potential and surface modifications of these two NPs. In addition, the wrapping of cell membranes also contributes to the difference in uptake between the two, as the presence of the cell membrane makes it easier for tumor cells to take up mFePCN by membrane fusion. Next, we synthesized NPs with dual fluorescence (FAM-FeP@si and FAM-mFeP@si) using FAM-labeled siRNA and further assessed the uptake of the NPs by 143B and K7M2 cells by CLSM 6 h after coincubation. Moreover, the commercial transfection reagent Lipomaster3000 (Vazyme, China) was used as a control to assess the ability of mFeP@si to deliver siRNA. There was no significant difference between mFeP@si and Lipomaster3000 in delivering siRNA to 143B cells, as evidenced by the distribution of green fluorescence inside the cells (Fig. 3C). K7M2 cells exhibited similar results (Fig. 3D). Moreover, from the CLSM image of FAM-mFeP@si, we confirmed that the green and red fluorescence strongly overlapped, which means that the spatial positions of FePCN and siRNA were highly overlapped, proving the successful synthesis of mFeP@si.

After being taken up by cells, most nanodrugs undergo intracellular transport via the endosomal-lysosomal pathway. Failed lysosomal escape usually causes degradation of NPs [37]. Therefore, overcoming the endosomal/lysosomal barrier is crucial for successful delivery of mFeP@si and OS treatment. The commercial reagent LysoTracker Green (Beyotime, China) was used to label intracellular lysosomes. We evaluated whether the NPs could achieve lysosomal escape in 143B and K7M2 cells by CLSM and colocalization analysis (ImageJ, USA). For 143B cells, in the absence of US irradiation, intracellular red and green fluorescence strongly overlapped, indicating that the NPs were localized in lysosomes, as evidenced by fluorescence colocalization analysis.

Interestingly, there was no significant overlap of intracellular red and green fluorescence under US irradiation, and in addition, the Pearson's correlation coefficients decreased from 0.88 to 0.41. Combined with CLSM images and colocalization analysis, mFeP@si successfully achieved lysosomal escape under US irradiation (Fig. 3E). K7M2 cells exhibited the same results under US irradiation, as demonstrated by CLSM images and colocalization analysis (Fig. 3F). Subsequently, we also examined the expression level of GPX4 at the protein level by Western Blot to show consistency. The results showed that the GPX4 gene silencing efficiency was obviously enhanced under US irradiation (Fig. S13). These results indicate that our synthesized NPs, which can be effectively taken up by OS cells and overcome the endosomal/lysosomal barrier, are promising for further applications. The mechanism of lysosomal escape is outlined in Fig. 3G. Briefly, $^1\text{O}_2$ produced by the synergistic effect of US, FePCN, and O_2 disrupts endosomal/lysosomal membranes to achieve lysosomal escape of mFeP@si.

3.4. Effects and mechanisms of synergistic therapy against OS

When used for biomedical applications, the toxicity and biocompatibility of NPs are characteristics that must be considered [38]. Therefore, we treated 293T (human) and L929 (mouse) cells with different concentrations of mFeP@si to assess biosafety in vitro. As shown in Fig. S14, cell viability remained above 90 % when the concentration of mFeP@si was less than 100 $\mu\text{g}/\text{mL}$. This trend, which remained consistent among the two cell lines, demonstrated the good biocompatibility of mFeP@si. For NPs administered via systemic routes for gene delivery, imaging and therapeutic purposes, blood compatibility is another safety issue that needs to be emphasized [39]. In vitro hemolysis experiments demonstrated that mFeP@si has good blood compatibility, and concentrations up to 400 $\mu\text{g}/\text{mL}$ did not cause significant hemolysis (Fig. S15). This finding undoubtedly indicates that mFeP@si has excellent biosafety and can be injected intravenously for therapeutic use. In theory, our synthesized mFeP@si can meet the needs of siGPX4-targeted delivery and SDT sensitization. When mFeP@si is taken up by OS cells, under US irradiation, the whole nanosystem amplifies the intracellular ROS storm, depletes GSH in various ways, and ultimately induces ferroptosis of tumor cells by inhibiting the function of GPX4. Therefore, we performed a series of in vitro experiments to evaluate the therapeutic effect on OS. A Calcein/PI cell viability/cytotoxicity Assay Kit (Beyotime, China) was used to assess the effect of different treatments on OS cell viability according to the manufacturer's guidelines (green fluorescence: live cells, red fluorescence: dead cells). As shown in Fig. 4A, compared to the control, naked siRNA and mFePCN had little effect on 143B and K7M2 cell viability, and only a few cells were stained red. This finding also proves the biosafety of mFePCN from another aspect. Under US irradiation, mFePCN killed some of the cells. Surprisingly, with the successful delivery of siGPX4 by mFeP@si, synergistic therapy with SDT and RNAi killed the vast majority of OS cells, as evidenced by the dense red fluorescence in the inverted fluorescence microscopy images. A colony formation assay was used to further confirm the tumor-suppressive effects of synergistic therapy in vitro (Fig. 4B). Compared with those in the other groups, only a small number of cell colonies were formed in the G5 (US + mFePCN) and G6 (US + mFeP@si) groups, and even fewer were formed in the G6 group. To further evaluate the tumor therapy efficacy, we also assessed 143B and K7M2 cell viability after different treatments by CCK-8 assay. Cell viability was markedly decreased in the G4, G5 and G6 groups, and the synergistic therapy with RNAi and SDT most significantly inhibited the viability of 143B and K7M2 cells (Fig. S16). Combined with the results above, we confirmed that the synergistic therapy of SDT and RNAi has a strong inhibitory effect on OS in vitro.

However, the pathway by which synergistic therapy inhibits OS progression remains unclear. Next, we explored the intrinsic mechanisms of synergistic therapy against OS in a variety of ways. Given the clear SDT and siGPX4 delivery abilities of mFeP@si, we first evaluated

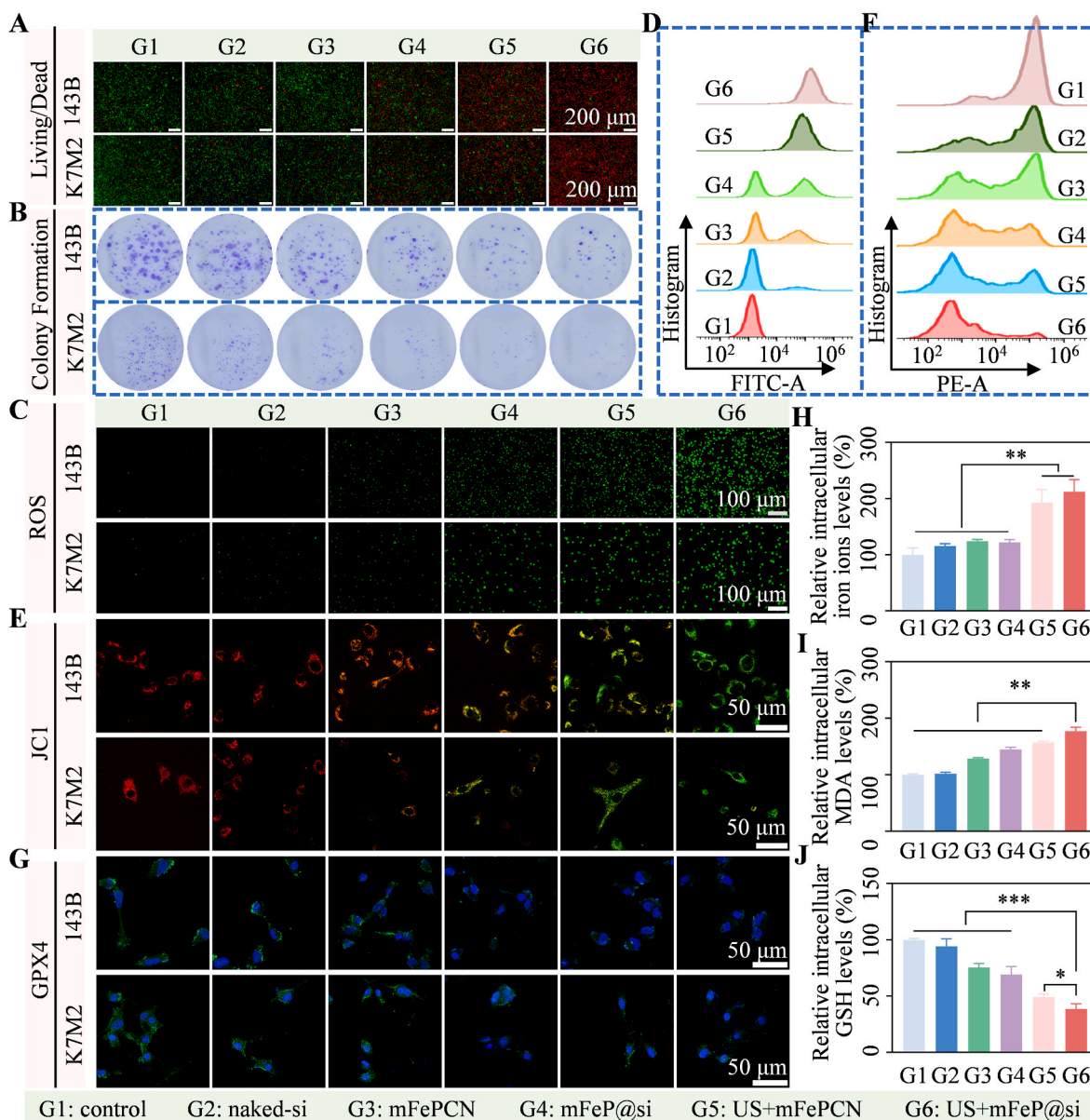


Fig. 4. A-B) Live and dead cell staining and colony formation of 143B and K7M2 cells after different treatments (scale bar: 200 μm). C) Fluorescence images of ROS levels in 143B and K7M2 cells after different treatments (scale bar: 100 μm). D) FCM results of ROS levels in 143B cells after different treatments. E) CLSM images of MMP loss in 143B and K7M2 cells after different treatments (scale bar: 50 μm). F) FCM results of MMP loss in 143B cells after different treatments. H) Relative intracellular iron ion levels, I) MDA levels, and J) GSH levels in 143B cells after different treatments. $n = 3$, * $p < 0.05$, ** $p < 0.01$, *** $p < 0.001$. G1: control; G2: naked-si; G3: mFePCN; G4: mFeP@si; G5: US + mFePCN; G6: US + mFeP@si.

the effects of different treatments on intracellular ROS levels in 143B and K7M2 cells via the use of a DCFH-DA probe. In the absence of additional stimulation, intracellular ROS were maintained at low levels, such as in the G1 (control) and G2 (naked-si) groups, and only a small amount of green fluorescence was observed in the cells. This is well explained because naked siRNA is negatively charged and can hardly be taken up by cells [40]. In the G3 (mFePCN) and G4 (mFeP@si) groups, the intracellular ROS levels increased, which may be related to the Fenton reaction induced by iron ions. Under US irradiation, cellular ROS levels were significantly elevated in the G5 (US + mFePCN) group, which could be explained by a significant effect of SDT. With the inhibition of GPX4 function, the intracellular antioxidant system further collapsed, and the synergistic therapy of SDT and RNAi maximized the increase in intracellular ROS levels in the G6 (US + mFeP@si) group (Fig. 4C). To further confirm these results, we also assessed intracellular ROS levels in different groups of 143B cells by FCM (Fig. 4D). Recent

studies have shown that loss of the mitochondrial membrane potential (MMP) is associated with cell death induced by SDT [41]. Therefore, we next evaluated MMP loss in different groups of cells by using a mitochondrial membrane potential assay kit (JC-1) (Beyotime, China). There was no significant loss of MMP in the G1 and G2 groups, as shown in the CLSM images, as evidenced by the bright red intracellular fluorescence. The MMP of cells in the G3 and G4 groups was partially lost, but overall, red fluorescence was still predominant. Under US irradiation, synergistic therapy with SDT and RNAi resulted in an almost complete loss of MMP in the G6 group, as evidenced by bright green intracellular fluorescence (Fig. 4E). Moreover, we evaluated the effect of different treatments on the mitochondrial membrane potential of 143B cells by FCM, and the results were consistent with those of CLSM (Fig. 4F). Moreover, we found reduced expression of GPX4 in the G4 and G5 groups by CLSM, which may be caused by siGPX4 and SDT-mediated GSH depletion, respectively. The most significant decrease in

intracellular GPX4 expression in the G6 group was attributed to the combination of siGPX4 and SDT (Fig. 4G).

ROS generation, MMP loss, and GPX4 inactivation are strongly associated with ferroptosis [42,43]. Ferroptosis, which is driven by lipid peroxidation, is an iron-dependent form of regulated cell death [44]. To clarify whether synergistic treatment inhibits OS progression by inducing ferroptosis, we first examined the levels of intracellular iron ions in 143B cells after different treatments (Fig. 4H). After US

irradiation, mFeP@si most significantly increased the intracellular iron ion concentration. However, the intracellular iron ion concentration in the G1-G4 groups remained almost unchanged. This apparent difference may be related to the elevated unstable iron pools in tumor cells. High levels of intracellular lipid peroxidation are thought to be a determinant of the onset of ferroptosis [45]. The detection of intracellular lipid peroxidation helps us to clarify whether ferroptosis occurs. Next, we detected the intracellular lipid peroxidation level in 143B cells with an

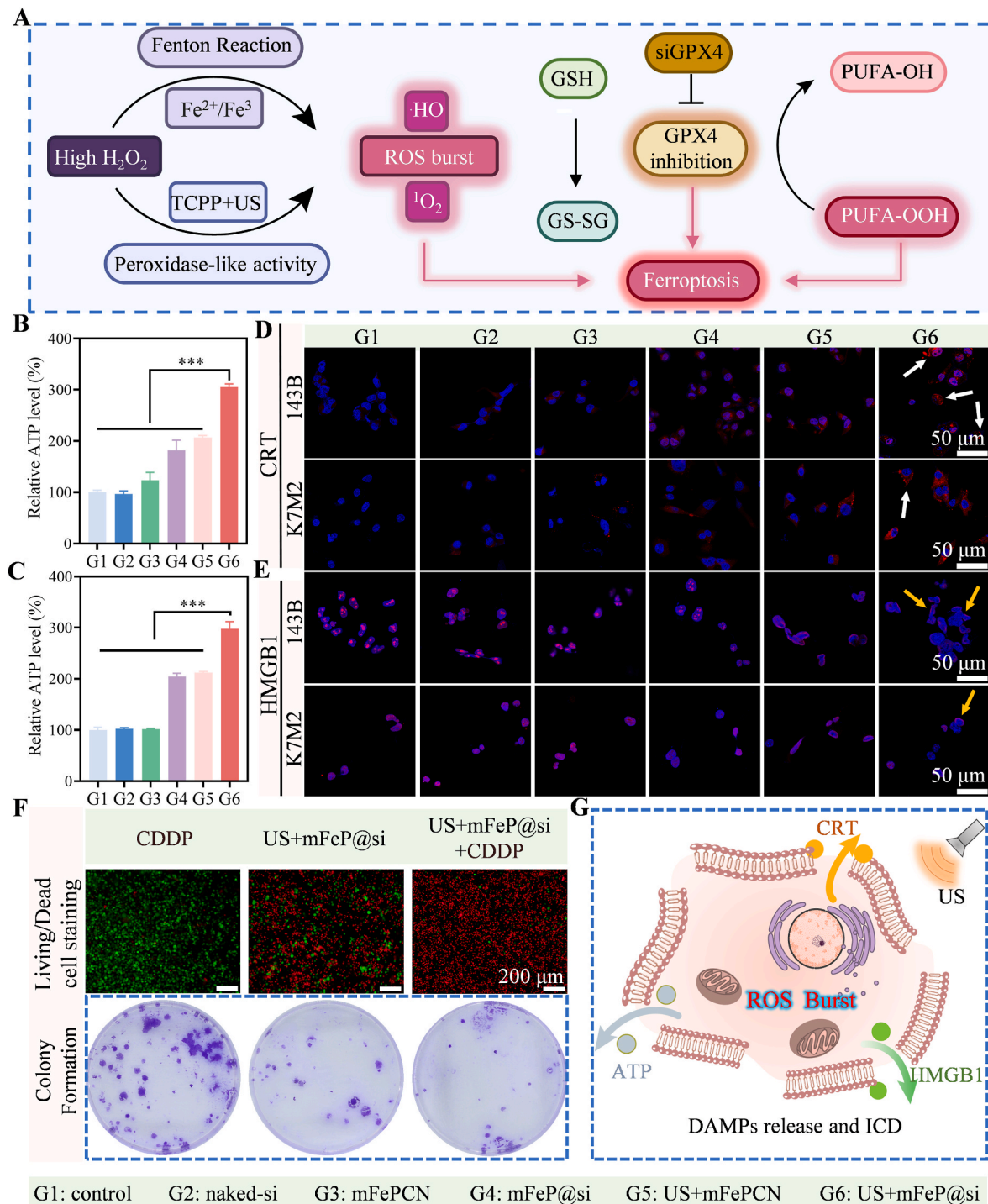


Fig. 5. A) Schematic illustration of robust ferroptosis triggered by RNAi and SDT. B–C) ATP concentration in the media of 143B and K7M2 cells ($n = 3$, $***p < 0.001$). D) CLSM images of surface-exposed CRT and E) released HMGB1 in 143B and K7M2 cells (Scale bar: 50 μm). F) Live and dead cell staining and colony formation in 143B-R cells after different treatments (Scale bar: 200 μm). G) Schematic illustration of synergistic treatment with RNAi and SDT to promote DAMPs (ATP, CRT, and HMGB1) release and ICD. G1: control; G2: naked-si; G3: mFePCN; G4: mFeP@si; G5: US + mFePCN; G6: US + mFeP@si.

MDA assay kit (Beyotime, China). As shown in Fig. 4I, compared with the other groups, the G6 group had the most pronounced accumulation of toxic lipid peroxidation, which was twice as high as that of the G1 group. Ferroptosis often occurs with GSH depletion, and GSH depletion in turn inactivates GPX4, leading to the accumulation of toxic lipid peroxidation products and further amplifying ferroptosis [46]. Therefore, the detection of intracellular GSH levels is important for assessing ferroptosis. For this purpose, a reduced GSH assay kit (Nanjing, China) was used to measure the level of GSH in 143B cells. Synergistic treatment with SDT and RNAi most significantly depleted intracellular GSH (Fig. 4J). In addition, we detected the same indicators of ferroptosis in K7M2 cells and obtained similar results (Fig. S17). These results demonstrated that the synergistic therapy with RNAi and SDT precisely triggered ferroptosis in OS cells of different species origin. Taken together, these results confirm our hypothesis presented in Fig. 5A. In brief, synergistic therapy with SDT and RNAi precisely boosts ferroptosis and ultimately inhibits OS progression by amplifying ROS storms, GSH depletion, GPX4 inactivation, and toxic lipid peroxidation accumulation.

3.5. ICD and chemotherapy sensitization

The immunosuppressive TME of OS is a challenge that has plagued researchers for years, as it has led to poor OS immunotherapy [47]. Therefore, developing therapeutic modalities that improve the immunosuppressive TME is essential for treating OS. Immunogenic cell death (ICD) is effectively triggered by the release of damage-associated molecular patterns (DAMPs), such as secreted adenosine triphosphate (ATP), surface-exposed calreticulin (CRT), and released high mobility group protein 1 (HMGB1), and stimulates the immune system to respond and elicit cytotoxic effects via antitumor immunity [48]. To assess whether synergistic treatment could trigger ICD, we examined the release of DAMPs from OS cells after different treatments. Extracellular ATP is an important “find me” signal for dendritic cells (DCs) and macrophages by binding to the purinergic receptor P2Y2 (P2RY2). Through NLRP3 inflammasome activation and interleukin 1 beta (IL-1 β) secretion, extracellular ATP mediates pro-inflammatory effects and ultimately leads to the activation of CD8⁺ T cells and $\gamma\delta$ T cells [49,50]. Therefore, an Enhanced ATP Assay Kit (Beyotime, China) was used to assess ATP release from 143B and K7M2 cells. Different treatments stimulated ATP secretion to some extent. Satisfactorily, the synergistic treatment of US + mFeP@si could maximally stimulate the secretion of ATP from the two OS cell lines, and the ATP concentration in the medium supernatant was three times greater than that in the control group (Fig. 5B and C). This significant difference in ATP secretion may be due to pre-mortem autophagy, resulting from mFeP@si and US-mediated RNAi/SDT/ferroptosis [51]. CRT, which is exposed to the surface of tumor cell membranes, acts as an “eat me” signal. By binding to LDL receptor-related protein 1 (LRP1, best known as CD91), CRT promotes phagocytosis of dying cells and corpses by DCs, further initiating T-cell-mediated antitumor immunity [52]. Therefore, we assessed surface-exposed CRT on the membranes of 143B and K7M2 cells after different treatments by using CLSM (Fig. 5D). After treatments, both cells showed different levels of surface-exposed CRT, as evidenced by the increasing red fluorescence in the CLSM images. The surface-exposed CRT was most pronounced in the 143B cells in G6, as illustrated by the white arrows in Fig. 5D. HMGB1 is an abundant nuclear protein that regulates the transcriptional activity of multiple proteins [53]. Before being released into the extracellular space by tumor cells undergoing ICD, HMGB1 needs to translocate from the nucleus to the cytoplasm first [54]. By binding to receptors such as Toll-like receptor 4 (TLR4), extracellularly released HMGB1 stimulates intrinsic immune cells and produces pro-inflammatory factors, further inducing intense inflammation [55]. Therefore, we assessed the intracellular localization of HMGB1 in 143B and K7M2 cells after different treatments by CLSM (Fig. 5E). In G1 to G3 groups, the red and green fluorescence in

the CLSM images were highly overlapped, suggesting that HMGB1 was located inside the nucleus and had not yet been released to the extracellular space. The localization of HMGB1 in the nucleus was reduced in some cells of the G4 group. Surprisingly, under US irradiation, the expression of HMGB1 in the G5 and G6 groups was significantly decreased, especially in G6 group, only a small amount of HMGB1 was distributed around the nucleus in the cells (as shown by the yellow arrows in Fig. 5E). These results suggested that HMGB1 was released into the extracellular space under the synergistic treatment with SDT and RNAi. The above results demonstrate that by amplifying the ROS storm and targeting ferroptosis, synergistic treatment with SDT and RNAi successfully triggered DAMP release and ICD to improve the TME of OS, which provides a new strategy for OS immunotherapy.

Chemotherapy resistance is a major adverse factor affecting the therapeutic efficacy of OS and the prognosis of patients and has plagued clinicians for many years [56]. Therefore, it is necessary to explore whether synergistic therapy can improve chemotherapy resistance in OS patients. Cisplatin-resistant 143B cells were induced by gradually increasing the concentration of cisplatin (CDDP) in the culture medium until 2 $\mu\text{g}/\text{mL}$ and named 143B-R. Similar to previous experiments, we evaluated the inhibition of 143B-R by CDDP, US + mFeP@si, and CDDP + US + mFeP@si by using live and dead cell staining and colony formation assays. As shown in Fig. 5F, CDDP alone was ineffective against 143B-R cells. Due to its ability to induce ferroptosis and immunogenic cell death in tumor cells, mFeP@si + US killed most of the 143B-R cells, but a portion of the 143B-R cells still survived. Notably, the combination of CDDP and mFeP@si + US killed almost all 143B-R cells. These results demonstrate that synergistic treatment with SDT and RNAi can enhance the sensitivity of cisplatin-resistant 143B-R cells to CDDP and has promising synergistic therapeutic potential. This is also supported by the results of colony formation experiments. Improving chemotherapy resistance is likely related to the large amount of ROS induced intracellularly by synergistic treatment [14]. In addition, inactivation of GPX4 may also lead to enhanced sensitivity of 143B-R cells to CDDP [57,58]. Fig. 5G briefly illustrates the application of synergistic therapy with SDT and RNAi for DAMP release and ICD induction.

3.6. Distribution in vivo

All the above in vitro experiments proved that mFeP@si can effectively deliver siGPX4, induce ferroptosis to kill OS cells and trigger ICD to improve the immunosuppressive TME. Next, we explored the anti-tumor effects of mFeP@si in vivo. For nanoparticles administered via the systemic route, possessing high cell-targeting specificity to avoid off-target effects and improve therapeutic efficacy is essential for successful treatment. Therefore, we utilized the fluorescence properties of FePCN to assess the in vivo distribution of the NPs in a subcutaneous OS model (established with K7M2 cells) at predesigned timepoints (0 h, 2 h, 4 h, 8 h, 12 h, and 24 h) after administration via tail vein injection with an animal imaging system (IVIS Lumina XRMS, PerkinElmer, USA). BALB/c mice with subcutaneous tumor volumes up to 100 mm^3 were randomly divided into three groups and treated with saline, FeP@si or mFeP@si, respectively. At 48 h, the mice were euthanized and autopsied to assess the accumulation of NPs in the heart, liver, spleen, lungs, kidneys and tumor. As shown in Fig. 6B, mice treated with saline did not show significant fluorescence throughout the preset time points. With time, FeP@si gradually accumulated at the tumor site, which could be explained by the enhanced permeability and retention (EPR) effect. Notably, although FeP@si also accumulated in the tumor, the fluorescence intensity and accumulation rate of mFeP@si were significantly greater than those of FeP@si. At each predetermined timepoint, the accumulation of mFeP@si, which was greater than that at the previous timepoint, reached a maximum at 24 h. In comparison, the accumulation of FeP@si at 24 h was approximately equivalent to the accumulation of mFeP@si at 6–12 h. The superior tumor targeting ability of mFeP@si is strongly associated with the homologous targeting ability

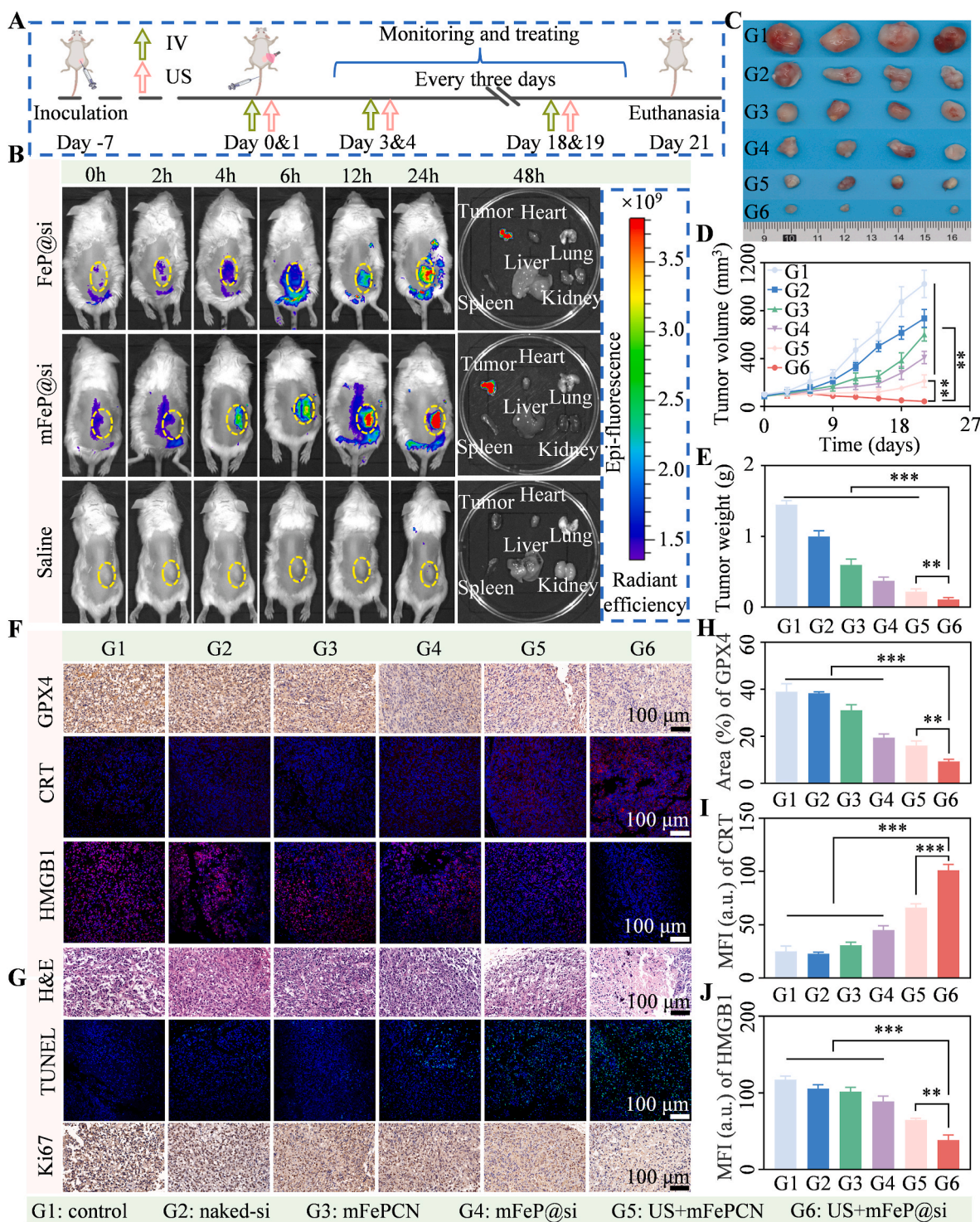


Fig. 6. A) Schematic illustration of antitumor therapeutic procedures in vivo. B) Distribution of FeP@si and mFeP@si in vivo assessed by IVIS after systemic administration. C) Digital camera photos of tumor specimens from all treatment groups. D) Changes of tumor volumes over time in all groups (n = 3, **p < 0.01). E) tumor weights at day 21 in all groups (n = 3, **p < 0.01, ***p < 0.001). F) Assessment ferroptosis induction (represented by IHC images of GPX4) and ICD induction (represented by IF images of CRT and HMGB1) after different treatments in vivo (Scale bar: 100 μm). G) H&E staining images, TUNEL images, and Ki67 IHC images of tumor sections from all treatment groups (Scale bar: 100 μm). H) Area (%) of GPX4 in all groups after different treatments. H) Mean Fluorescent Intensity (MFI) of CRT and J) HMGB1 in all groups (n = 3, **p < 0.01, ***p < 0.001). G1: control; G2: naked-si; G3: mFePCN; G4: mFeP@si; G5: US + mFePCN; G6: US + mFeP@si.

provided by the tumor cell membrane. Based on the existence of variable adhesion molecules on the surface (such as galactoglucan-3, E-cadherin, and mucin), tumor cell membranes provide superior self-recognition and self-adhesion capabilities for efficient tumor targeting [59]. These results indicate that the cell membrane coating has a

profound impact on the tumor targeting ability of the NPs and confirm the outstanding tumor targeting ability of mFeP@si.

3.7. Anti-OS effects of mFeP@si in vivo

Inspired by the outstanding antitumor effects, we next investigated the anti-OS effects of different treatments in vivo through a subcutaneous tumor model in BALB/c nude mice established with 143B cells. Fig. 6A briefly illustrates the tumor xenograft model establishment and treatment procedure in vivo. Briefly, 24 h after intravenous injection, the nude mice were exposed to US irradiation, which was repeated every three days, and euthanized on day 21. Tumor specimens were used for histological analyses to assess tumor necrosis, ferroptosis induced by GPX4 inactivation, and DAMPs release; blood and major organs were used to assess the biosafety and organ toxicity of the NPs. Body weights and tumor volumes were monitored every three days throughout the treatment procedures. BALB/c nude mice with tumor volume up to 100 mm³ were randomized into six groups (G1: control; G2: naked-si; G3: mFePCN; G4: mFeP@si; G5: US + mFePCN; G6: US + mFeP@si) and subjected to different treatments. Fig. 6C shows digital camera photos of all tumor specimens. mFePCN alone retarded tumor growth, probably because FePCN released iron ions and induced the Fenton reaction in a slightly acidic environment. Compared with mFePCN, mFeP@si had a more pronounced therapeutic effect, and in addition to the Fenton reaction, the inactivation of GPX4 mediated by siGPX4 and thus inducing ferroptosis played a role in inhibiting OS progression. Surprisingly, under US irradiation, tumor progression was significantly inhibited in the G5 and G6 groups, and the tumor volumes in the G6 group were reduced by approximately 50 % compared with those in the pretreatment group. These results are consistent with the changes in tumor volume and weight (Fig. 6D and E). The body weights of the nude mice remained stable throughout the treatment period (Fig. S18), indicating that all these therapeutic regimens had negligible detrimental effects on the animals.

As shown in Fig. 6F, tumor sections were used to confirm the occurrence of ferroptosis (by immunohistochemical staining of GPX4) and ICD (by immunofluorescence staining of CRT and HMGB1). Compared with the G1 group, there was little difference in the expression of GPX4 in G2 and G3 groups. GPX4 expression was decreased in the G4 group, and this decrease was caused by siGPX4 delivery in vivo. Unexpectedly, GPX4 expression was also reduced in the G5 group. This might be ascribed to the depletion of GSH by the large amount of ROS induced by FePCN-mediated enhanced SDT, which in turn suppressed the expression of GPX4. Consistent with our findings, GPX4 expression was most significantly suppressed in the G6 group, which was attributed to siGPX4 delivery and enhanced SDT-mediated GSH depletion. GPX4 IHC analysis also corroborated these results (Fig. 6H). Consistent with the results of the cell experiments, both the G5 and G6 groups, effectively induced surface exposure of CRT and release of HMGB1, which was particularly apparent in the G6 group and was indicated by increased red fluorescence on the cell surface and decreased red fluorescence in the cells, respectively. Mean fluorescence intensity (MFI) analysis of CRT and HMGB1 supported these results (Fig. 6I and J). Taken together, these results revealed that synergistic treatment with SDT and RNAi inhibited OS growth and progression and improved the immunosuppressive TME in vivo by inducing ferroptosis and ICD. The most severe cell necrosis was found in G6, as evidenced by pyknosis, karyorrhexis, and karyolysis in hematoxylin and eosin (H&E) staining. Tumor tissues in the G6 group underwent the most obvious apoptosis, as confirmed by terminal deoxynucleotidyl transferase dUTP nick end labeling (TUNEL) immunofluorescence staining (green fluorescence). Ki67 immunohistochemical staining is widely used to estimate tumor proliferation. US + mFeP@si led to the greatest reduction in the quantity of Ki67-positive cells, demonstrating its excellent ability to inhibit OS invasion (Fig. 6G). In addition, mice blood and major organs (heart, lung, liver, spleen, and kidneys) were used to evaluate the biosafety and toxicity of in vivo treatments, respectively. Blood analysis and H&E staining of major organs further confirmed the biosafety of the NPs (Figs. S19 and S20).

4. Conclusion

Current therapies for OS have hit a bottleneck, survival for patients has remained almost the same over the past 30 years, and there is an urgent need for new therapies to increase therapeutic efficacy. Here, we conceived and manufactured a TME-responsive FePCN-based biomimetic nanosystem (named mFeP@si) with RNAi and SDT to inhibit OS growth and invasion in vitro and in vivo. Under US irradiation, FePCN achieved tandem catalysis from H₂O₂ to O₂ and O₂ to ¹O₂, which ameliorated tumor hypoxia, enhanced SDT, and achieved lysosomal escape. Enhanced SDT aggravated intracellular oxidative stress and led to an intracellular ROS storm, GSH was thus compensatorily depleted and in turn, inactivated GPX4 to some extent. Moreover, siGPX4 was precisely bound to mRNA and mediated its degradation. With the inactivation of GPX4, lipid hydroperoxides could not be reduced to the corresponding alcohols and accumulated in cells. Ultimately, irreversible ferroptosis mediated robust anti-OS effects. Synergistic therapy with RNAi and SDT also maximized the triggering of ICD and alleviated the immunosuppressive TME. In addition, this synergistic treatment produced unexpected results in cisplatin-resistant OS cells and increased OS sensitivity to cisplatin. In general, our rigorous work provides new perspectives for treating OS and is promising for improving patient prognosis.

CRedit authorship contribution statement

Ningxiang Sun: Writing – original draft, Methodology, Investigation, Conceptualization. **Qingjian Lei:** Writing – original draft, Methodology, Investigation, Conceptualization. **Meng Wu:** Writing – original draft, Methodology, Investigation, Conceptualization. **Shijie Gao:** Methodology, Investigation. **Zhiqiang Yang:** Methodology. **Xuan Lv:** Methodology. **Renxiong Wei:** Writing – original draft, Supervision, Methodology, Funding acquisition, Conceptualization. **Feifei Yan:** Writing – original draft, Supervision, Methodology, Funding acquisition, Conceptualization. **Lin Cai:** Writing – original draft, Supervision, Methodology, Funding acquisition, Conceptualization.

Declaration of competing interest

The authors declare the following financial interests/personal relationships which may be considered as potential competing interests: Feifei Yan reports financial support was provided by Zhongnan Hospital of Wuhan University. Renxiong Wei reports financial support was provided by Department of Science and Technology of Hubei Province. Meng Wu reports financial support was provided by Department of Science and Technology of Hubei Province. We thank the Medical Science Research Center, Zhongnan Hospital, Wuhan University and the Experimental Teaching Center of Basic Medical Sciences, Wuhan University, for technical support. If there are other authors, they declare that they have no known competing financial interests or personal relationships that could have appeared to influence the work reported in this paper.

Data availability

Data will be made available on request.

Acknowledgments

This work was funded by the Program of Excellent Doctoral (Post-doctoral) of Zhongnan Hospital of Wuhan University (Grant No. ZNYB2021005) and Key R&D Programs of Hubei Province (Grant No. 2023BCB024 and 2022BCA032). We thank the Medical Science Research Center, Zhongnan Hospital, Wuhan University and the Experimental Teaching Center of Basic Medical Sciences, Wuhan University, for their technical support.

Appendix A. Supplementary data

Supplementary data to this article can be found online at <https://doi.org/10.1016/j.mtbo.2024.101053>.

References

- J. Gill, R. Gorlick, Advancing therapy for osteosarcoma, *Nat. Rev. Clin. Oncol.* 18 (10) (2021) 609–624, <https://doi.org/10.1038/s41571-021-00519-8>.
- P.S. Meltzer, D.L. Longo, L.J. Helman, New horizons in the treatment of osteosarcoma, *N. Engl. J. Med.* 385 (22) (2021) 2066–2076, <https://doi.org/10.1056/NEJMr2103423>.
- J. Ritter, S.S. Bielack, Osteosarcoma, *Ann. Oncol.* 21 (Suppl 7) (2010), <https://doi.org/10.1093/annonc/mdq276.vii320-5>.
- G. Lei, L. Zhuang, B. Gan, Targeting ferroptosis as a vulnerability in cancer, *Nat. Rev. Cancer* 22 (7) (2022) 381–396, <https://doi.org/10.1038/s41568-022-00459-0>.
- C. Liang, X. Zhang, M. Yang, X. Dong, Recent progress in ferroptosis Inducers for cancer therapy, *Adv. Mater.* 31 (51) (2019) 1904197, <https://doi.org/10.1002/adma.201904197>.
- F. Zeng, S. Nijjati, L. Tang, J. Ye, Z. Zhou, X. Chen, Ferroptosis detection: from approaches to applications, *Angew. Chem., Int. Ed. Engl.* 62 (35) (2023) e202300379, <https://doi.org/10.1002/anie.202300379>.
- Z. Shen, T. Liu, Y. Li, J. Lau, Z. Yang, W. Fan, Z. Zhou, C. Shi, C. Ke, V.I. Bregadze, S.K. Mandal, Y. Liu, Z. Li, T. Xue, G. Zhu, J. Munasinghe, G. Niu, A. Wu, X. Chen, Senton-reaction-acceleratable Magnetic nanoparticles for ferroptosis therapy of orthotopic brain tumors, *ACS Nano* 12 (11) (2018) 11355–11365, <https://doi.org/10.1021/acsnano.8b06201>.
- B.R. Stockwell, Ferroptosis turns 10: emerging mechanisms, physiological functions, and therapeutic applications, *Cell* 185 (14) (2022) 2401–2421, <https://doi.org/10.1016/j.cell.2022.06.003>.
- Z. Xu, L. Chen, C. Wang, L. Zhang, W. Xu, MicroRNA-1287-5p promotes ferroptosis of osteosarcoma cells through inhibiting GPX4, *Free. Radic. Res.* 55 (11–12) (2021) 1119–1129, <https://doi.org/10.1080/10715762.2021.2024816>.
- A. Kumar, A. Singam, G. Swaminathan, N. Killi, N.K. Tangudu, J. Jose, R. Gundloori Vn, L. Dinesh Kumar, Combinatorial therapy using RNAi and curcumin nano-architectures regresses tumors in breast and colon cancer models, *Nanoscale* 14 (2) (2022) 492–505, <https://doi.org/10.1039/D1NR04411G>.
- S.M. Hoy, Parisian: first global approval, *Drugs* 78 (15) (2018) 1625–1631, <https://doi.org/10.1007/s40265-018-0983-6>.
- L.J. Scott, Givosiran: first approval, *Drugs* 80 (3) (2020) 335–339, <https://doi.org/10.1007/s40265-020-01269-0>.
- S. Son, J.H. Kim, X. Wang, C. Zhang, S.A. Yoon, J. Shin, A. Sharma, M.H. Lee, L. Cheng, J. Wu, J.S. Kim, Multifunctional sonosensitizers in sonodynamic cancer therapy, *Chem. Soc. Rev.* 49 (11) (2020) 3244–3261, <https://doi.org/10.1039/c9cs00648f>.
- Y. Li, Y. Liu, J. Xu, D. Chen, T. Wu, Y. Cao, Macrophage–cancer hybrid membrane-camouflaged nanoplatforms for HIP-1 α gene silencing-enhanced sonodynamic therapy of glioblastoma, *ACS Appl. Mater. Interfaces* 15 (26) (2023) 31150–31158, <https://doi.org/10.1021/acsmi.3c03001>.
- Q. Xu, G. Zhan, Z. Zhang, T. Yong, X. Yang, L. Gan, Manganese porphyrin-based metal-organic framework for synergistic sonodynamic therapy and ferroptosis in hypoxic tumors, *Theranostics* 11 (4) (2021) 1937–1952, <https://doi.org/10.7150/thno.45511>.
- M.X. Wu, Y.W. Yang, Metal-organic framework (MOF)-Based drug/cargo delivery and cancer therapy, *Adv. Mater.* 29 (23) (2017), <https://doi.org/10.1002/adma.201606134>.
- Z. Chen, K.O. Kirlikovali, L. Shi, O.K. Farha, Rational design of stable functional metal-organic frameworks, *Mater. Horiz.* 10 (9) (2023) 3257–3268, <https://doi.org/10.1039/d3mh00541k>.
- S. Yuan, L. Feng, K. Wang, J. Pang, M. Bosch, C. Lollar, Y. Sun, J. Qin, X. Yang, P. Zhang, Q. Wang, L. Zou, Y. Zhang, L. Zhang, Y. Fang, J. Li, H.C. Zhou, Stable metal-organic frameworks: design, synthesis, and applications, *Adv. Mater.* 30 (37) (2018) e1704303, <https://doi.org/10.1002/adma.201704303>.
- Q. Ren, N. Yu, L. Wang, M. Wen, P. Geng, Q. Jiang, M. Li, Z. Chen, Nanoarchitectonics with metal-organic frameworks and platinum nanozymes, *J. Colloid Interface Sci.* 614 (2022) 147–159, <https://doi.org/10.1016/j.jcis.2022.01.050>.
- J. Zhuang, H. Gong, J. Zhou, Q. Zhang, W. Gao, R.H. Fang, L. Zhang, Targeted gene silencing in vivo by platelet membrane-coated metal-organic framework nanoparticles, *Sci. Adv.* 6 (13) (2020) eaaz6108, <https://doi.org/10.1126/sciadv.aaz6108>.
- L. Guo, S. Zhong, P. Liu, M. Guo, J. Ding, W. Zhou, Radicals scavenging MOFs enabling targeting delivery of siRNA for rheumatoid arthritis therapy, *Small* 18 (27) (2022) e2202604, <https://doi.org/10.1002/smll.202202604>.
- S. Zeng, Q. Tang, M. Xiao, X. Tong, T. Yang, D. Yin, L. Lei, S. Li, Cell membrane-coated nanomaterials for cancer therapy, *Mater. Today. Bio.* 20 (2023) 100633, <https://doi.org/10.1016/j.mtbo.2023.100633>.
- F. Raza, H. Zafar, S. Zhang, Z. Kamal, J. Su, W.E. Yuan, Q. Mingfeng, Recent advances in cell membrane-derived biomimetic nanotechnology for cancer immunotherapy, *Adv. Healthcare Mater.* 10 (6) (2021) e2002081, <https://doi.org/10.1002/adhm.202002081>.
- Y. Li, F. Li, H. Pan, X. Huang, J. Yu, X. Liu, Q. Zhang, C. Xiao, H. Zhang, L. Zhang, Targeted OUM1/PTPRZ1 silencing and synergetic CDT/enhanced chemical therapy toward uveal melanoma based on a dual-modal imaging-guided manganese metal-organic framework nanoparticles, *J. Nanobiotechnol.* 20 (1) (2022) 472, <https://doi.org/10.1186/s12951-022-01643-y>.
- H. Yu, Y. Li, Z. Zhang, J. Ren, L. Zhang, Z. Xu, Y. Kang, P. Xue, Silk fibroin-capped metal-organic framework for tumor-specific redox dyshomeostasis treatment synergized by deoxygenation-driven chemotherapy, *Acta Biomater.* 138 (2022) 545–560, <https://doi.org/10.1016/j.actbio.2021.11.009>.
- L. Jiao, G. Wan, R. Zhang, H. Zhou, S.H. Yu, H.L. Jiang, From metal-organic frameworks to single-atom Fe implanted N-doped porous carbons: efficient oxygen reduction in both alkaline and acidic media, *Angew. Chem., Int. Ed. Engl.* 57 (28) (2018) 8525–8529, <https://doi.org/10.1002/anie.201803262>.
- S. Li, X. Chen, S. Guan, Z. Wang, W. Cao, G. Luo, X. Ling, Precisely amplifying intracellular oxidative storm by metal-organic coordination polymers to augment anticancer immunity, *ACS Nano* 17 (15) (2023) 15165–15179, <https://doi.org/10.1021/acsnano.3c04785>.
- X.-F. Bai, Y. Chen, M.-Z. Zou, C.-X. Li, Y. Zhang, M.-J. Li, S.-X. Cheng, X.-Z. Zhang, Homotypic targeted photosensitive nanointerferer for tumor cell cycle arrest to boost tumor photoimmunotherapy, *ACS Nano* 16 (11) (2022) 18555–18567, <https://doi.org/10.1021/acsnano.2c06871>.
- P. Resnier, T. Montier, V. Mathieu, J.P. Benoit, C. Passirani, A review of the current status of siRNA nanomedicines in the treatment of cancer, *Biomaterials* 34 (27) (2013) 6429–6443, <https://doi.org/10.1016/j.biomaterials.2013.04.060>.
- A.K. Varkouhi, M. Scholte, G. Storm, H.J. Haisma, Endosomal escape pathways for delivery of biologicals, *J. Contr. Release* 151 (3) (2011) 220–228, <https://doi.org/10.1016/j.jconrel.2010.11.004>.
- P.-J. Lou, P.-S. Lai, M.-J. Shieh, A.J. MacRobert, K. Berg, S.G. Bown, Reversal of doxorubicin resistance in breast cancer cells by photochemical internalization, *Int. J. Cancer* 119 (11) (2006) 2692–2698, <https://doi.org/10.1002/ijc.22098>.
- B. Hassannia, P. Vandenabeele, T. Vanden Berghe, Targeting ferroptosis to iron out cancer, *Cancer Cell* 35 (6) (2019) 830–849, <https://doi.org/10.1016/j.ccell.2019.04.002>.
- C. He, K. Lu, D. Liu, W. Lin, Nanoscale metal-organic frameworks for the Co-delivery of cisplatin and pooled siRNAs to enhance therapeutic efficacy in drug-resistant ovarian cancer cells, *J. Am. Chem. Soc.* 136 (14) (2014) 5181–5184, <https://doi.org/10.1021/ja4098862>.
- M. Sönksen, K. Kerl, H. Bunzen, Current status and future prospects of nanomedicine for arsenic trioxide delivery to solid tumors, *Med. Res. Rev.* 42 (1) (2022) 374–398, <https://doi.org/10.1002/med.21844>.
- L.A. Mulcahy, R.C. Pink, D.R. Carter, Routes and mechanisms of extracellular vesicle uptake, *J. Extracell. Vesicles* 3 (2014), <https://doi.org/10.3402/jev.v3.24641>.
- R.H. Fang, W. Gao, L. Zhang, Targeting drugs to tumours using cell membrane-coated nanoparticles, *Nat. Rev. Clin. Oncol.* 20 (1) (2023) 33–48, <https://doi.org/10.1038/s41571-022-00699-x>.
- J. Gilleron, W. Querbes, A. Zeigerer, A. Borodovsky, G. Marsico, U. Schubert, K. Manyoats, S. Seifert, C. Andree, M. Stöter, H. Epstein-Barash, L. Zhang, V. Kotelianskiy, K. Fitzgerald, E. Fava, M. Bickle, Y. Kalaidzidis, A. Akinc, M. Maier, M. Zerial, Image-based analysis of lipid nanoparticle-mediated siRNA delivery, intracellular trafficking and endosomal escape, *Nat. Biotechnol.* 31 (7) (2013) 638–646, <https://doi.org/10.1038/nbt.2612>.
- C. Zhang, J. Lu, F. Tian, L. Li, Y. Hou, Y. Wang, L. Sun, X. Shi, H. Lu, Regulation of the cellular uptake of nanoparticles by the orientation of helical polypeptides, *Nano Res.* 12 (4) (2019) 889–896, <https://doi.org/10.1007/s12274-019-2319-6>.
- S. Guo, Y. Shi, Y. Liang, L. Liu, K. Sun, Y. Li, Relationship and improvement strategies between drug nanocarrier characteristics and hemocompatibility: what can we learn from the literature, *Asian J. Pharm. Sci.* 16 (5) (2021) 551–576, <https://doi.org/10.1016/j.ajps.2020.12.002>.
- M. Zoulikha, Q. Xiao, G.F. Bofo, M.A. Sallam, Z. Chen, W. He, Pulmonary delivery of siRNA against acute lung injury/acute respiratory distress syndrome, *Acta, Der Pharm. Sin. B.* 12 (2) (2022) 600–620, <https://doi.org/10.1016/j.apsb.2021.08.009>.
- X. Sun, H. Xu, J. Shen, S. Guo, S. Shi, J. Dan, F. Tian, Y. Tian, Y. Tian, Real-time detection of intracellular reactive oxygen species and mitochondrial membrane potential in THP-1 macrophages during ultrasonic irradiation for optimal sonodynamic therapy, *Ultrason. Sonochem.* 22 (2015) 7–14, <https://doi.org/10.1016/j.ulsonch.2014.06.016>.
- S. Wei, T. Qiu, X. Yao, N. Wang, L. Jiang, X. Jia, Y. Tao, Z. Wang, P. Pei, J. Zhang, Y. Zhu, G. Yang, X. Liu, S. Liu, X. Sun, Arsenic induces pancreatic dysfunction and ferroptosis via mitochondrial ROS-autophagy-lysosomal pathway, *J. Hazard Mater.* 384 (2020) 121390, <https://doi.org/10.1016/j.jhazmat.2019.121390>.
- M. Gao, J. Yi, J. Zhu, A.M. Minikes, P. Monian, C.B. Thompson, X. Jiang, Role of mitochondria in ferroptosis, *Mol. Cell.* 73 (2) (2019) 354–363.e3, <https://doi.org/10.1016/j.molcel.2018.10.042>.
- X. Chen, R. Kang, G. Kroemer, D. Tang, Broadening horizons: the role of ferroptosis in cancer, *Nat. Rev. Clin. Oncol.* 18 (5) (2021) 2080–2096, <https://doi.org/10.1038/s41571-020-00462-0>.
- M.K. Foret, R. Lincoln, S. Do Carmo, A.C. Cuello, G. Cosa, Connecting the "dots": from free radical lipid oxidation to cell pathology and disease, *Chem. Rev.* 120 (23) (2020) 12757–12787, <https://doi.org/10.1021/acs.chemrev.0c00761>.
- S.J. Dixon, D.N. Patel, M. Welsch, R. Skouta, E.D. Lee, M. Hayano, A.G. Thomas, C. E. Gleason, N.P. Tatonetti, B.S. Slusher, B.R. Stockwell, Pharmacological inhibition of cystine-glutamate exchange induces endoplasmic reticulum stress and ferroptosis, *Elife* 3 (2014) e02523, <https://doi.org/10.7554/eLife.02523>.
- Z. Zhang, W. Ji, J. Huang, Y. Zhang, Y. Zhou, J. Zhang, Y. Dong, T. Yuan, Q. Yang, X. Ding, L. Tang, H. Li, J. Yin, Y. Wang, T. Ji, J. Fei, B. Zhang, P. Chen, H. Hu, Characterization of the tumour microenvironment phenotypes in malignant tissues

- and pleural effusion from advanced osteoblastic osteosarcoma patients, *Clin. Transl. Med.* 12 (11) (2022) e1072, <https://doi.org/10.1002/ctm2.1072>.
- [48] K. Hayashi, F. Nikolos, Y.C. Lee, A. Jain, E. Tsouko, H. Gao, A. Kasabyan, H. E. Leung, A. Osipov, S.Y. Jung, A.V. Kurtova, K.S. Chan, Tipping the immunostimulatory and inhibitory DAMP balance to harness immunogenic cell death, *Nat. Commun.* 11 (1) (2020) 6299, <https://doi.org/10.1038/s41467-020-19970-9>.
- [49] F. Ghiringhelli, L. Apetoh, A. Tesniere, L. Aymeric, Y. Ma, C. Ortiz, K. Vermaelen, T. Panaretakis, G. Mignot, E. Ullrich, J.L. Perfettini, F. Schlemmer, E. Tasdemir, M. Uhl, P. Génin, A. Civas, B. Ryffel, J. Kanellopoulos, J. Tschopp, F. André, R. Lidereau, N.M. McLaughlin, N.M. Haynes, M.J. Smyth, G. Kroemer, L. Zitvogel, Activation of the NLRP3 inflammasome in dendritic cells induces IL-1beta-dependent adaptive immunity against tumors, *Nat. Med.* 15 (10) (2009) 1170–1178, <https://doi.org/10.1038/nm.2028>.
- [50] I. Martins, Y. Wang, M. Michaud, Y. Ma, A.Q. Sukkurwala, S. Shen, O. Kepp, D. Métivier, L. Galluzzi, J.L. Perfettini, L. Zitvogel, G. Kroemer, Molecular mechanisms of ATP secretion during immunogenic cell death, *Cell Death Differ.* 21 (1) (2014) 79–91, <https://doi.org/10.1038/cdd.2013.75>.
- [51] L. Galluzzi, I. Vitale, S. Warren, S. Adjemian, P. Agostinis, A.B. Martinez, T. A. Chan, G. Coukos, S. Demaria, E. Deutsch, D. Draganov, R.L. Edelson, S. C. Formenti, J. Fucikova, L. Gabriele, U.S. Gaip, S.R. Gameiro, A.D. Garg, E. Golden, J. Han, K.J. Harrington, A. Hemminki, J.W. Hodge, D.M.S. Hossain, T. Illidge, M. Karin, H.L. Kaufman, O. Kepp, G. Kroemer, J.J. Lasarte, S. Loi, M. T. Lotze, G. Manic, T. Merghoub, A.A. Melcher, K.L. Mossman, F. Prosper, Ø. Rekdal, M. Rescigno, C. Riganti, A. Sistigu, M.J. Smyth, R. Spisek, J. Stagg, B. E. Strauss, D. Tang, K. Tatsuno, S.W. van Gool, P. Vandenabeele, T. Yamazaki, D. Zamarin, L. Zitvogel, A. Cesano, F.M. Marincola, Consensus guidelines for the definition, detection and interpretation of immunogenic cell death, *J. Immunother. Cancer.* 8 (1) (2020), <https://doi.org/10.1136/jitc-2019-000337>.
- [52] L. Kasikova, M. Hensler, I. Truxova, P. Skapa, J. Laco, L. Belicova, I. Praznovec, S. Vosahlikova, M.J. Halaska, T. Brtnicky, L. Rob, J. Presl, J. Kostun, I. Cremer, A. Ryska, G. Kroemer, L. Galluzzi, R. Spisek, J. Fucikova, Calreticulin exposure correlates with robust adaptive antitumor immunity and favorable prognosis in ovarian carcinoma patients, *J. Immunother. Cancer* 7 (1) (2019) 312, <https://doi.org/10.1186/s40425-019-0781-z>.
- [53] D.V. Krysko, A.D. Garg, A. Kaczmarek, O. Krysko, P. Agostinis, P. Vandenabeele, Immunogenic cell death and DAMPs in cancer therapy, *Nat. Rev. Cancer* 12 (12) (2012) 860–875, <https://doi.org/10.1038/nrc3380>.
- [54] H. Yang, H. Wang, S.S. Chavan, U. Andersson, High mobility group box protein 1 (HMGB1): the prototypical endogenous danger molecule, *Mol. Med.* 21 (Suppl 1) (2015) S6–s12, <https://doi.org/10.2119/molmed.2015.00087>, Suppl 1.
- [55] P. Scaffidi, T. Misteli, M.E. Bianchi, Release of chromatin protein HMGB1 by necrotic cells triggers inflammation, *Nature* 418 (6894) (2002) 191–195, <https://doi.org/10.1038/nature00858>.
- [56] J. Tang, G. Duan, Y. Wang, B. Wang, W. Li, Z. Zhu, Circular RNA ANKIB1 accelerates chemo-resistance of osteosarcoma via binding microRNA-26b-5p and modulating enhancer of zeste homolog 2, *Bioengineered* 13 (3) (2022) 7351–7366, <https://doi.org/10.1080/21655979.2022.2037869>.
- [57] Z. Zhu, Y. Zheng, H. He, L. Yang, J. Yang, M. Li, W. Dai, H. Huang, FBXO31 sensitizes cancer stem cells-like cells to cisplatin by promoting ferroptosis and facilitating proteasomal degradation of GPX4 in Liver, *Inter* 42 (12) (2022) 2871–2888, <https://doi.org/10.1111/liv.15462>.
- [58] Q. Liu, K. Wang, The induction of ferroptosis by impairing STAT3/Nrf2/GPx4 signaling enhances the sensitivity of osteosarcoma cells to cisplatin, *Cell Biol. Int.* 43 (11) (2019) 1245–1256, <https://doi.org/10.1002/cbin.11121>.
- [59] D. Fan, Y. Cao, M. Cao, Y. Wang, Y. Cao, T. Gong, Nanomedicine in cancer therapy, *Signal Transduct. Targeted Ther.* 8 (1) (2023) 293, <https://doi.org/10.1038/s41392-023-01536-y>.